JGR Atmospheres

RESEARCH ARTICLE
10.1029/2019JD030845

Key Points:
- Annual evaporation shows considerable interannual variability, with decreasing trend occurs throughout 2003–2016 over majority Southern Ocean
- The sea ice concentration and skin temperature play a large role in the magnitude and interannual variance of fall, spring, and mean evaporation
- Largest increasing trends occur in the Ross Sea in JJA and DJF

Correspondence to:
L. Boisvert,
linette.n.boisvert@nasa.gov

Citation:
Boisvert, L., Vihma, T., & Shie, C.-L. (2020). Evaporation from the Southern Ocean estimated on the basis of AIRS satellite data. *Journal of Geophysical Research: Atmospheres*, *125*, e2019JD030845. https://doi.org/10.1029/2019JD030845

Received 17 APR 2019
Accepted 14 DEC 2019
Accepted article online 19 DEC 2019

Evaporation From the Southern Ocean Estimated on the Basis of AIRS Satellite Data

Linette Boisvert[1], Timo Vihma[2], and Chung-Lin Shie[3]

[1]Cryospheric Sciences Lab, NASA Goddard Space Flight Center, Greenbelt, MD, USA, [2]Finnish Meteorological Institute, Helsinki, Finland, [3]Joint Center for Earth Systems Technology (JCET), University of Maryland, Baltimore County, Baltimore, MD, USA

Abstract Evaporation plays an important role in the global water and energy cycles and, hence, in climate change. Evaporation over the Southern Ocean, where the Antarctic sea ice coverage has a large annual cycle, is poorly quantified. In this study, daily evaporation is estimated for the Southern Ocean with a sea-ice-specific algorithm, using surface temperature and air humidity from National Aeronautics and Space Administration's Atmospheric Infrared Sounder (AIRS), and wind speeds from Modern-Era Retrospective Analysis for Research and Applications, Version 2 (MERRA-2), reanalysis during 2003–2016. An uncertainty of 34% was found in the evaporation product. The results indicate that annual evaporation has considerable interannual and regional variability, but with a decreasing trend during the study period over most of the Southern Ocean. There are, however, areas where evaporation has increased, specifically in the Ross Sea in winter and summer, with smaller positive trends in spring and fall. Overall, the changes in the difference between the surface specific humidity and the air specific humidity, and to a much lesser extent in the wind speed, are the main drivers for the changes in evaporation throughout the year. During spring and fall months, changes to the sea ice cover, which alter the surface specific humidity, are the main drivers for the change, but in summer and winter the main driver is the air-specific humidity. Air masses originating from the Antarctic continent (south) are associated with cold and dry conditions, which increase evaporation, whereas air masses from lower latitudes in the Southern Ocean (north) are associated with warm and moist conditions, decreasing evaporation. Comparisons with other reanalysis evaporation products produce similar trends, although annual averages differ.

1. Introduction

Sea ice modulates the interaction between the underlying ocean surface and the atmosphere above. Sea ice and the snowpack on top of the ice are strong reflectors of solar radiation (Perovich & Polashenski, 2012) and efficient insulators, prohibiting the exchange of heat and moisture between the atmosphere and ocean (Pringle et al., 2007). Changes to the sea ice area, concentration, and thickness can thus alter these exchanges. These changes can then affect both local and global surface energy budgets via the fluxes of solar shortwave and thermal longwave radiation and turbulent fluxes of sensible and latent heat (Bourassa et al., 2013). The latent heat flux is related to evaporation or sublimation from the ocean or ice/snow surface to the atmosphere or to condensation of atmospheric moisture on the surface. Evaporation and sublimation increase the air specific humidity, and the increased water vapor can condense and lead to cloud or fog formation, thus altering the downwelling longwave and shortwave radiation at the surface and the amount radiated back to space (Wyser et al., 2008).

Since water vapor is a strong greenhouse gas, it also contributes to climate warming (Rinke et al., 2009; Serreze et al., 2009). A warming atmosphere and increasing net heat flux at the surface enhance melting of the sea ice pack (Taylor et al., 2018), which in turn could allow for increased evaporation, generating a positive feedback loop. Changes in evaporation also impact the global water cycle and freshwater budget (Huntington, 2006; Loaiciga et al., 1996; Trenberth, 1999) potentially leading to changing precipitation amounts and patterns (Bintanja & Selten, 2014). Evaporation is also important for the salinity and water mass formation in the Southern Ocean. Although precipitation exceeds evaporation practically everywhere over the Southern Ocean (Tietäväinen & Vihma, 2008), evaporation reduces the freshening of surface waters caused by precipitation. Without evaporation, there would be less formation of deep and bottom water in the Weddell Sea (Gordon, 1971).

As the sea ice in both the Arctic and Antarctic is changing rapidly, the associated changes in evaporation and precipitation are potentially very important in modulating climate change. The most striking change witnessed is the decline in Arctic sea ice extent since it has been continuously monitored by satellites beginning in the late 1970s (Parkinson & Cavalieri, 2008; Parkinson & DiGirolamo, 2016). More recently, since the early 2000s, the sea ice has experienced an increased rate of decline in extent and thickness (Serreze & Meier, 2018), switching to a seasonal first-year dominated ice pack (Maslanik et al., 2011; Nghiem et al., 2007) compared to the sea ice of the 1980–1990s (e.g., Comiso et al., 2008; Kwok & Rothrock, 2009; Lindsay & Schweiger, 2015). This loss in sea ice coverage has allowed for the ocean surface and atmosphere to interact in regions and seasons when sea ice previously prohibited such exchanges. Due to these changes, it was found that evaporation from the Arctic Ocean has increased (Boisvert et al., 2015) and the Arctic has become warmer and wetter (Boisvert & Stroeve, 2015; Vihma et al., 2016), with indications of increased cloudiness, predominantly in low clouds in autumn (Eastman & Warren, 2010; Kay & Gettelman, 2009; Liu et al., 2012; Palm et al., 2010). It is important to note that changes in sea ice are not necessarily responsible for changes in Arctic clouds in other seasons, specifically summer (Kay & Gettelman, 2009; Morrison et al., 2018; Taylor et al., 2015).

Changes to the Antarctic sea ice over the satellite record have not been as drastic as in the Arctic, however (Parkinson & Cavalieri, 2012; Parkinson & DiGirolamo, 2016). In fact, Antarctic sea ice had experienced a modest increasing trend up until 2015 (Maksym, 2019). Since then extents have been anomalously low, eluding to changing atmospheric and oceanic drivers of the sea ice surrounding Antarctica. The Antarctic sea ice extent is thought to be controlled by many factors including the ocean surface temperatures (Comiso, 2016), the opening, and the depletion of the stratospheric ozone layer, which has contributed to stronger westerlies and positive phase of the Southern Annular Mode (SAM; Turner et al., 2015), and atmospheric circulation changes related to El Niño–Southern Oscillation (ENSO; Zhang, 2007; Kwok & Comiso, 2002). Due to these changing conditions, it is important to understand how, why, and if these changes are affecting evaporation/sublimation from the Southern Ocean, which is important to the global climate system.

A few studies have looked at turbulent fluxes of heat and moisture in the Southern Ocean focusing either on short-term polynya events (Kottmeier & Engelbart, 1992) or estimating the fluxes using in situ measurements from various cruises and buoys. For example, Vihma et al. (2002) computed the turbulent fluxes of sensible and latent heat from the Weddell Sea using buoy observations, along with various other data and compared the results with reanalysis data, but only for one year: 1996. Other short-term studies, Andreas and Makshats (1985) during 1981, Andreas et al. (2000) during 1992, and Vihma et al. (2009) in early summer 2004, calculated turbulent fluxes using research cruise and drifting ice station measurements taken in the Weddell Sea. Wendler et al. (2005) took flux measurements from a cruise in 2000/2001 in the Ross Sea toward McMurdo. Moore et al. (2002) looked at the turbulent fluxes using National Centers for Environmental Prediction (NCEP) reanalysis data from the Weddell Polynya during the 1974 event. While the majority of these previous works were very important in understanding the turbulent energy exchange in the Weddell Sea, they are confined to just one region of the Antarctic sea ice pack and might not be representative of the turbulent fluxes elsewhere (Vihma et al., 2009). Field campaigns with a limited duration do not allow analyses of long-term changes in the fluxes of heat and moisture, so that quantitative knowledge on these turbulent fluxes in the Southern Ocean remains very limited.

So far there have been no studies specifically looking at evaporation on a large spatial and temporal scale, nor using remotely sensed data to estimate evaporation in the Southern Ocean. This work aims to fill this knowledge gap, by producing daily estimates of evaporation from the Southern Ocean, partly covered by sea ice, during 2003–2016 using data from National Aeronautics and Space Administration (NASA)'s Atmospheric Infrared Sounder (AIRS).

2. Data

2.1. Atmospheric Infrared Sounder – AIRS

AIRS was chosen for this study because it has produced reasonable estimates of temperature and humidity over the Arctic Ocean (e.g., Boisvert et al., 2015) and the Southern Ocean (Dong et al., 2010). AIRS also has twice daily global coverage and produces accurate retrievals under most cloud conditions, which is important in the Southern Ocean where data are very sparse and clouds can be prevalent. Another advantage of

using AIRS is that estimates of evaporation are produced primarily using one instrument/satellite platform. This allows for the estimates to be more consistent in time and helps to alleviate biases that would be introduced with measurements taken at different times by different instruments.

AIRS data products have also been used to produce full daily coverage of Arctic Ocean evaporation that has been shown to be representative of the boundary conditions, when compared with in situ data and ERA-Interim, over the Arctic sea ice. Specifically, ERA-Interim had a 35% (15%) error in skin temperature (specific humidity) compared to AIRS with a 17% (18%) error in skin temperature (specific humidity; e.g., Boisvert et al., 2012, 2013; Boisvert, Wu, Vihma, & Susskind, 2015; Boisvert, Wu, & Shie, 2015). AIRS data have also performed well over the Greenland Ice Sheet, with errors of 2 K (0.34 g/kg) in skin temperature (specific humidity) when compared with GC-Net and Programme for Monitoring of the Greenland Ice Sheet weather stations. From these findings, AIRS data have also been used to estimate evaporation over the Greenland ice sheet and were found to compare well with a regional climate model, having annual differences between 30 $\pm$ 15% overall, being smaller in the interior of the ice sheet (Boisvert et al., 2016). In a study by Dong et al. (2010), AIRS reproduced more representative turbulent fluxes when compared with other available gridded products in relation to ship borne measurements in the Southern Ocean; however, this was not undertaken in the sea ice pack but in the Drake Passage.

The AIRS instrument on NASA's Aqua satellite was launched in May 2002 and is still currently operational. AIRS is a cross-track high spectral resolution infrared sounder with 2,378 infrared channels that collect data with a 13.5-km spatial resolution in the horizontal at nadir. Quality controlled geophysical products of the Earth and its atmosphere are generated by the AIRS science team (Susskind et al., 2014). The algorithm also utilizes a cloud-clearing radiance approach, where the surface and atmospheric retrievals are iterated to best fit the final cloud-cleared radiances. For more information on the AIRS retrieval algorithm see Susskind et al. (2014).

In this study daily evaporation between 1 January 2003 and 31 December 2016 is estimated using AIRS level 3 version 6 skin temperature, air temperature, relative humidity, and geopotential heights from 1,000- and 925-hPa pressure levels. The geopotential heights are used to determine the actual height of the 925- and 1,000-hPa pressure levels above sea level. Evaporation also depends on the wind speed, which is taken from a reanalysis (see below).

2.2. NASA's Modern-Era Retrospective Analysis for Research and Application, Version 2 – MERRA-2

MERRA-2 (Gelaro et al., 2017) is a global reanalysis produced by NASA's Global Modeling and Assimilation Office (GMAO) and is an update of the MERRA (Rienecker et al., 2011) reanalysis system, with output fields available from 1980 to the present. As compared with MERRA, MERRA-2 employs an updated 3-D-variational assimilation system with an Incremental Analysis Update and has a comparable grid spacing of 69 km (Bosilovich et al., 2016; Molod et al., 2015). But prior to output, computations are performed on a cubed-sphere grid to better resolve Polar regions. Sea ice concentrations use the daily sea surface temperature product of Reynolds et al. (2007) until April 2006 and the Operational Sea Surface Temperature and Sea Ice Analysis (OSTIA) thereafter. MERRA-2 daily 10-m wind speeds from 1 January 2003 until 31 December 2016 are applied with AIRS products to estimate evaporation in this study.

In addition, MERRA-2 2-m air temperature and specific humidity are used for comparisons with AIRS and buoy data. Although MERRA-2 assimilates AIRS clear-sky only retrievals, the method for producing AIRS atmospheric variables (e.g., Susskind et al., 2014) is very different from how MERRA-2 ingests AIRS radiances. Therefore, MERRA-2 and AIRS humidities at 925- and 1,000-hPa levels are rather independent (see Figure 2c).

2.3. Sea Ice Concentration

Daily sea ice concentration data are retrieved from the Special Sensor Microwave Imager/Sounder (SSMIS) on the Defense Meteorological Satellite Program (DMSP)-F13 satellite for 2003–2007 and the DMSP-F17 satellite for 2008–2016 (Cavalieri et al., 1996, updated yearly).

All data are transposed onto the 25-km^2 polar stereographic Antarctic grid from the National Snow and Ice Data Center (NSIDC) for ease of comparison and calculations of the evaporation. Southern Ocean regions

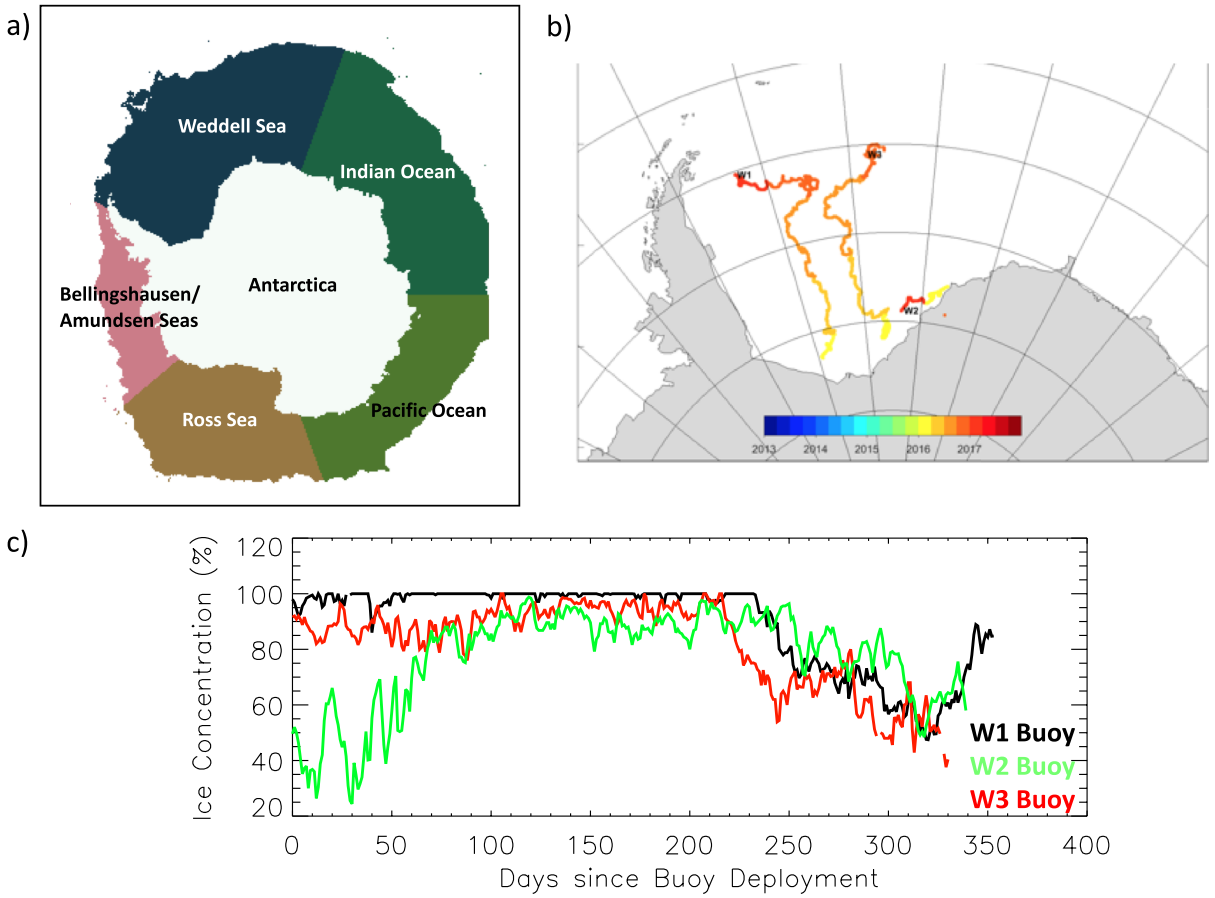

Figure 1. (a) Ocean region map for the Southern Ocean. Sea ice extent, which does not vary in time, used in evaporation and other calculations is highlighted in each region. The white areas are not included. Region mask taken from nsidc.org. (b) Antarctic weather buoy tracks for 2016W1, 2016W2, and 2016W3 buoys located in the Weddell Sea. Figure taken from meereisportal.de. (c) Daily ice concentration at the closest latitude and longitude of each buoy since the start of its deployment. All buoys have lower ice concentration at the end of their deployment (in December 2016) where a larger amount of open water would influence the Atmospheric Infrared Sounder (AIRS) return with its larger footprint than the buoy measurement.

are defined using the region mask also taken from NSIDC and shown in Figure 1a. A sea ice mask is applied to all of the averages and trends in evaporation and other variables in order to not include those areas of the Southern Ocean where sea ice has never been present during our study period. The ice mask is produced including all grid points where sea ice concentration has exceeded 15% in any day during 2003–2016. The extent of the sea ice mask is shown in Figure 1a.

3. Method

Evaporation (E) is estimated using the same methodology as described in detail in Boisvert et al., 2013; Boisvert, Wu, Vihma, & Susskind, 2015], where E ($\mathrm{kg \cdot m^{-2} \cdot s^{-1}}$) is defined as the vertical surface flux of water vapor due to atmospheric turbulent transport. It is computed from the difference in specific humidity between the surface, whether it be sea ice or ice-free ocean, and the air, as well as the factors that affect the intensity of the turbulent exchange: wind speed, surface roughness, and thermal stratification (Launiainen & Vihma, 1994).

$$E = \rho S_r \left[I_c C_{Ez,i} \left(q_{s,i} - q_z \right) + (1 - I_c) C_{Ez,w} \left(q_{s,w} - q_z \right) \right] \tag{1}$$

In (1), ρ is the air density ($\mathrm{kg/m^3}$), S_r is the effective wind speed (m/s), $C_{ez,i(w)}$ is the water vapor transfer coefficient over ice (water; unitless), I_c is the ice concentration (%), $q_{s,i(w)}$ is the saturation specific humidity at the

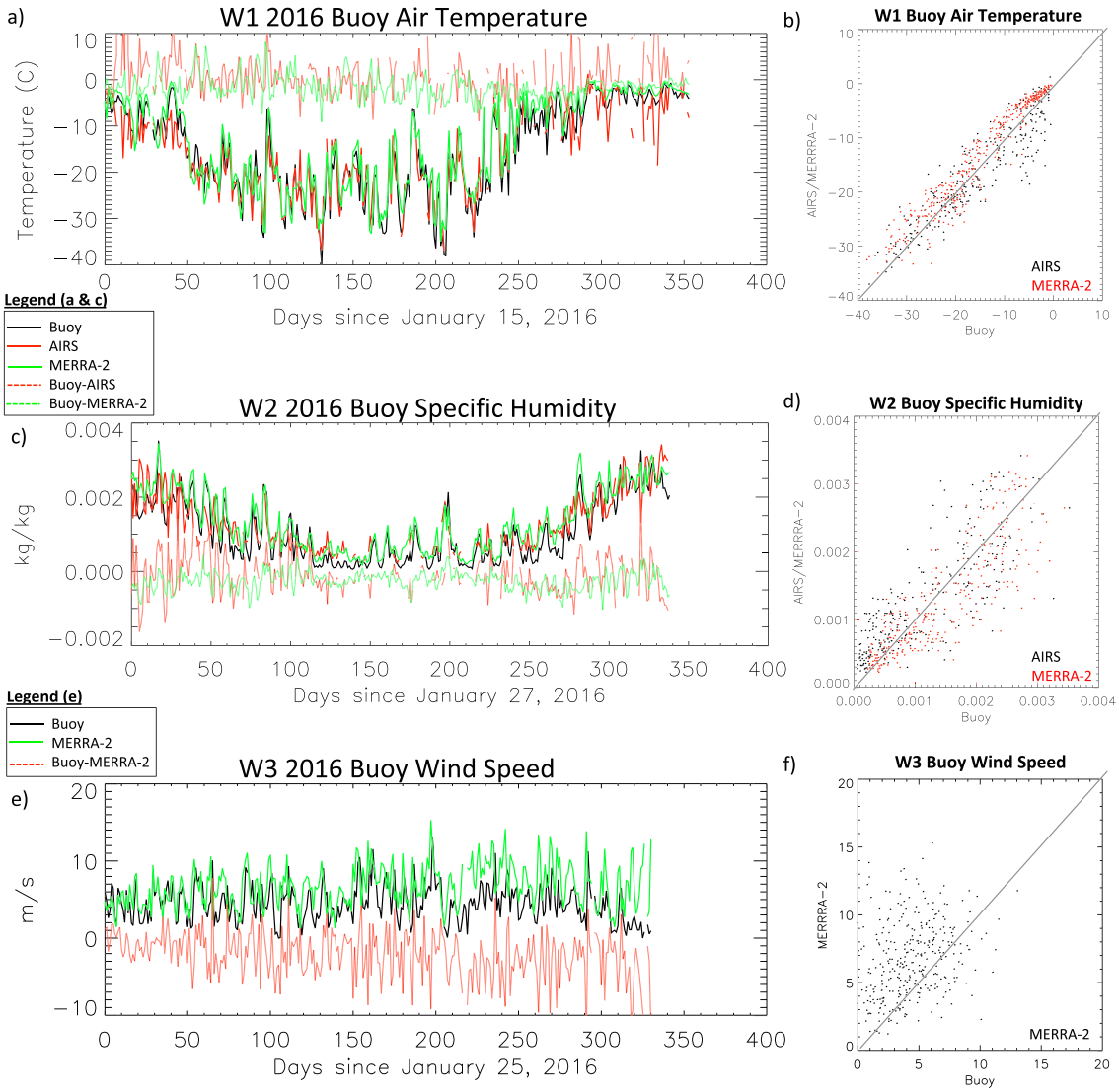

Figure 2. Ice Mass Balance Buoys from the Weddell Sea deployed in 2016 and comparisons with Atmospheric Infrared Sounder (AIRS) and Modern-Era Retrospective Analysis for Research and Applications, Version 2 (MERRA-2). Buoy tracks are shown in Figure 1b. (a) Air temperature time series with the W1 buoy temperature in black, AIRS in red, and MERRA-2 in green. The dashed lines represent the difference between the buoy and AIRS (red dashed) and the buoy and MERRA-2 (dashed green). (b) Scatterplot showing AIRS vs. W1 buoy (black dots) air temperatures and MERRA-2 vs. W1 buoy (red dots). (c) Same as for (a) except for specific humidity and the W2 buoy. (d) Same as (b) but for specific humidity and the W2 buoy. (e) Wind speed time series with the W3 buoy in black, adjusted 2-m MERRA-2 in green. The dashed red line represents the difference between the buoy and MERRA-2 wind speeds. (f) Same as for (b) but for wind speed and W3 buoy.

ice (water) surface (kg/kg), and q_z is the specific humidity at 2 m (kg/kg). According to (1), a positive flux (from the surface to air) represents evaporation or sublimation and a negative flux represents condensation.

S_r is calculated from the 10-m wind speed and includes a parameter for gustiness, which is different in stable and unstable conditions (Andreas et al., 2010). E is estimated from (1) using the bulk aerodynamic method and Monin-Obukhov similarity theory along with an iterative calculation scheme based on Launiainen and Vihma (1990), where multiple modifications have been made to better represent the boundary layer over the sea ice. These include the flux algorithm from Grachev et al. (2007) for stably stratified conditions over sea ice, and adjustments to the roughness lengths of sea ice in different seasons according to Andreas et al., 2010; Andreas, Persson, et al., 2010]. These modifications are thought to better represent the boundary layer over the sea ice and thus are unique from global reanalysis products, which assume the same boundary layer

parameterizations globally. In doing so they are probably not optimal for evaporation over sea ice (Bourassa et al., 2013; Grachev et al., 2007). For more details on these modifications see Boisvert et al., 2013; Boisvert, Wu, Vihma, & Susskind, 2015].

It is important to note that these sea ice parameterizations were produced on the basis of data collected from the Arctic sea ice zone during the Surface Heat Budget of the Arctic Ocean (SHEBA) campaign between 1997 and 1998 (Perovich et al., 1999). They are assumed to be applicable for the Antarctic sea ice zone, as the atmospheric boundary layer stability is the main factor in influencing the turbulent surface flux of water vapor. The stability dependence of the flux should not depend on the hemisphere. However, Arctic and Antarctic sea ice zones differ with respect to typical ice concentration (lower in the Antarctic), presence of melt ponds in summer (only in the Arctic), and occurrence of pressure ridges (more in the Arctic) and sastrugi (more in the Antarctic). These affect the aerodynamic and thermal roughness lengths, which further affect the turbulent flux of moisture (Andreas, 1995; Andreas, Horst, et al., 2010; Andreas, Persson, et al., 2010; Lüpkes & Gryanik, 2015). Until specific turbulent flux parameterizations are developed for the Antarctic sea ice zone, we consider it best to apply parameterizations based on data from Arctic sea ice, which are more representative than midlatitude parameterizations, like those widely used in reanalyses.

The iterative method (Launiainen & Vihma, 1990) allows for the use of the AIRS data at 925 and 1,000 hPa (i.e., air temperature, relative humidity, and geopotential height) and MERRA-2 10-m wind speed, which are all measured at varying heights, to be computed to their values at a standard reference height, in this case 2 m. Using information on the surface roughness, thermal stratification, and the height difference between the pressure levels and 2-m level, the AIRS variables are converted to 2-m level. If the geopotential height is below the surface, then the geopotential height is automatically set to 2 m. These adjusted 2-m variables are compared with in situ observations in the following section.

4. Assessment of Input Variables and Uncertainty Analysis

The skill of the 2-m adjusted AIRS temperature and humidity products are first assessed with in situ data and a global reanalysis, MERRA-2. MERRA-2 10-m and the adjusted 2-m wind speeds are also assessed with in situ data, as they are used in calculations of evaporation.

The accuracy of the AIRS-based air temperature and specific humidity converted to 2-m level is assessed using three ice mass balance buoys (Grosfeld et al., 2016; Nicolaus et al., 2017) deployed in the Weddell Sea in January 2016. These buoys, classified as W1, W2, and W3, collected air temperature, humidity, and wind speed data for roughly a year as they drifted on sea ice flows. Their drift tracks are shown in Figure 1b. While the buoy data are taken as the reference in this study, the instruments are still prone to erroneous measurements and uncertainties due to the harsh environment (Launiainen & Vihma, 1994). It is also important to keep in mind that point measurements from the buoys are compared with the closest footprint on the 25-km^2 polar stereographic grid for AIRS and MERRA-2 data and might be contaminated with ice-free ocean returns depending on the location.

Three examples of these comparisons are shown in Figure 2, specifically, the air temperature comparisons from W1, specific humidity from W2, and wind speed from W3, and the results from all comparisons made are summarized in Table 1. For all three buoys, both AIRS and MERRA-2 compare rather closely with the buoy temperatures, with the root-mean-square error (RMSE; averaged over the three buoys) being 4.6°C for AIRS and 3.6°C for MERRA-2. AIRS has a much smaller bias than MERRA-2, on average being slightly colder than the buoys, whereas MERRA-2 is warmer than the buoys (Table 1 and Figure 2a). It is interesting to note that the temperatures from AIRS tend to diverge and fluctuate widely at the end of 2016 for the W1 and W3 buoys, specifically when these buoys have moved to lower latitudes, and have entered the summer season. During this time, they are encountering a higher concentration of open water (Figure 1c), which is impacting the temperature of the larger footprint from AIRS. Overall, both AIRS and MERRA-2 also show good correlation with the buoy temperatures, having an average R-value of 0.80 and 0.95, respectively.

The specific humidity comparisons are similar to the temperature comparisons in that AIRS produces larger RMS errors compared to MERRA-2, with the average errors for all buoys of 4.7×10^{-4} kg/kg and 2.3×10^{-5} kg/kg, respectively (Table 1). AIRS also produces much smaller biases compared to MERRA-2. Again, AIRS tends to produce more varying results for the W1 and W3 buoys during the end of 2016, when these buoys

Table 1
Comparisons of Air Temperature, Humidity, and Wind Speed from AIRS and MERRA-2 With Ice Mass Balance Buoys in the Weddell Sea in 2016

Buoys	AIRS			MERRA-2		
	RMSE	Bias	Correlation	RMSE	Bias	Correlation
			Temperature (°C)			
W1	3.86	0.63	R=0.70	2.95	−1.51	R=0.96
W2	5.48	−0.54	R=0.84	5.02	−3.38	R=0.94
W3	4.54	0.87	R=0.87	2.82	−1.26	R=0.96
Average	4.63	0.32	R=0.80	3.60	−2.05	R=0.95
			Specific humidity (kg/kg)			
W1	$6.2x10^{-4}$	$-8.3x10^{-5}$	R=0.79	3.2×10^{-4}	-1.7×10^{-4}	R=0.96
W2	5.3×10^{-5}	-1.1×10^{-4}	R=0.80	3.6×10^{-5}	-2.6×10^{-4}	R=0.95
W3	7.5×10^{-4}	6.3×10^{-5}	R=0.72	3.4×10^{-4}	-9.4×10^{-5}	R=0.95
Average	4.74×10^{-4}	-4.3×10^{-5}	R=0.77	2.3×10^{-4}	-1.7×10^{-4}	R=0.95
			Wind speed (m/s)			
		2-m adjusted MERRA-2			10-m original MERRA-2	
W1	2.69	1.15	R=0.48	3.49	2.20	R=0.43
W2	2.90	1.11	R=0.50	3.78	2.16	R=0.45
W3	3.12	1.17	R=0.28	3.82	2.08	R=0.28
Average	2.90	1.14	R=0.42	3.70	2.15	R=0.39

Abbreviations: AIRS: Atmospheric Infrared Sounder; MERRA-2: Modern-Era Retrospective Analysis for Research and Applications, Version 2; RMSE: root-mean-square error.

had drifted northward, to areas of open water, which will affect the returns of the footprint. This is also witnessed with MERRA-2 data, but the magnitude of the variations was less. The correlations between the buoys and AIRS and MERRA-2 are also high, again showing that although the magnitudes might be slightly off between AIRS and MERRA-2, the day-to-day fluctuations are very similar.

MERRA-2 10-m wind speeds are used in the calculation of evaporation because presently, neither AIRS nor any other satellite product can measure the wind speeds over sea ice. Both 10-m and the adjusted 2-m MERRA-2 wind speeds and the buoy wind speeds were compared (Table 1), and the results with the W3 buoy are shown in Figures 2e and 2f. The 10-m wind speeds from MERRA-2 are always slightly higher than what the buoy records, with a bias of 2.1 m/s on average. This could be due to the height of the wind measurements of the buoy, which are most likely well below 10 m. In fact, the 2-m adjusted MERRA-2 wind speeds only have a 1.14 m/s bias on average and have a smaller RMSE than the 10-m wind speeds with 2.9 compared to 3.7 m/s (Table 1). Both the 10-m and 2-m wind speeds follow similar day-to-day variations with those of the buoys. However, the correlations of the wind speeds are significantly lower than those of the temperatures and humidities.

The robustness of the derived AIRS evaporation product and the results presented here depend on the accuracy of the input variables (e.g., AIRS skin temperature, relative humidity, and MERRA-2 wind speed) and the validity of the assumptions of the Monin Obukhov similarity theory. Uncertainties for the wind speed, specific humidity, and air density (the last one estimated using the uncertainty of the AIRS-based surface temperature) are taken from Table 1. An uncertainty of ±20% is taken for the water vapor transfer coefficient from Cronin et al. (2006). Average values of the calculated sensitivities, estimated uncertainties, and the final uncertainties for the Southern Ocean from 2003 to 2016 are shown in Table 2. We assumed that all of the variables are uncorrelated and this has allowed us to make an uncertainty estimate from (2)

$$\sigma_E^2 = \sum \sigma_x^2 \left(\frac{dE}{dx}\right)^2 = \sigma_\rho^2 \frac{dE^2}{d\rho} + \sigma_{C_E}^2 \frac{dE}{dC_E}^2 + \sigma_U^2 \frac{dE^2}{dU} + \sigma_{(q_s - q_z)}^2 \frac{dE}{d(q_s - q_z)}^2 \quad (2)$$

Using this method and the average uncertainty estimates of the variables in Table 2, an uncertainty of the evaporation product in the Southern Ocean was found to be 8.2×10^{-4} g · m^{-2} · s^{-1}, which equates to a 34% uncertainty overall when compared with the annual average evaporation from the Southern Ocean. This is not a large uncertainty when compared to the range of variability of evaporation in the Southern Ocean (~50%) during the 2003–2016 time period.

Table 2
Sensitivity of Evaporation Due to Different Input Uncertainties

Variable (x)	$\frac{dE}{dx}$	σ_x	$\sigma_x \frac{dE}{dx}$
ρ (g/m^3)	1.6×10^{-6} m/s	0.02	3.5×10^{-8} g · m^{-2} · s^{-1}
CE	1.0×10^{-3} g · m^{-2} · s^{-1}	3.2×10^{-4}	3.2×10^{-7} g · m^{-2} · s^{-1}
U (m/s)	2.6×10^{-7} g/m^3	2.9	7.5×10^{-7} g · m^{-2} · s^{-1}
qs-qa (g/kg)	2.0×10^{-5} g · m^{-2} · s^{-1}	4.7×10^{-4}	9.4×10^{-9} g · m^{-2} · s^{-1}
σ_E (g · m^{-2} · s^{-1})	8.2×10^{-4}		
$<E>$ (g · m^{-2} · s^{-1})	2.4×10^{-3}	Percent error	34%

Note. Values from this table are used in equation (2). σ_E indicates the standard deviation of the evaporation uncertainty and $<E>$ is the average annual evaporation from the Southern Ocean taken from Table 3.

Additional reasons why using the AIRS and MERRA-2 data and our method for estimating evaporation are beneficial include the following: (1) This derived evaporation dataset provides a new estimate with a relatively small uncertainty and combining these results with existing ones (e.g., reanalyses and operational analyses of numerical weather prediction models) provides additional material to evaluate the mean and scatter between different products of evaporation over the Southern Ocean. (2) AIRS is often underutilized in the Polar regions but could be a valuable asset where in situ measurements are sparse or nonexistent and atmospheric reanalyses have errors. Thus, it is of great importance to explore this new potential application of AIRS data. (3) In our method, as in Boisvert et al., 2013, the skin temperature and air humidity are always based on the same sensor onboard NASA's EOS Aqua satellite: AIRS. Although this derived evaporation does include errors, these are expected to be systematic rather than varying from year to year compared to the amount of observations assimilated into reanalyses, which varies depending on the availability of various in situ and remote sensing data. The performance of AIRS and MERRA-2 compared to the buoys and the error analysis performed demonstrate that (1) these data can be used confidently in producing evaporation estimates and 2) the spatial and interannual variations in evaporation and the results therein include reasonable patterns for the Southern Ocean.

5. Evaporation From the Southern Ocean

The average annual cycle of evaporation along with those for the sea ice area, wind speed, and specific humidity differences for the Southern Ocean between 2003 and 2016 are shown in Figure 3. In this figure, the Southern Ocean is split into four different sea ice regimes: (1) ice-free ocean (<15% ice concentration), (2) marginal sea ice (15-80% ice concentration), (3) sea ice pack (>80% ice concentration), and (4) entire ocean (0–100% ice concentration; encompassing all sea ice and ocean areas in the region mask outlined in Figure 1a) in order to distinguish the impact of the sea ice cover on the evaporation. Please note that the entire ocean regime (4) is made up of the average of each of the regimes (1–3); the area-averaging is based on the temporally varying number of grid points that make up each regime. The averaged monthly areas of each of the sea ice regimes are shown in Figure 3b. The entire ocean regime (black line) is constant because its area does not change in time and corresponds to the sea ice maximum area shown in Figure 1a.

Over the entire ocean regime (Figure 3a, black line), the evaporation is largest in the beginning of fall (March) with a minimum in the winter (June), having an average of 4.6×10^{-3} and 1.3×10^{-3} g · m^{-2} · s^{-1}, respectively (Table 3). The evaporation decreases in winter and then increases to a second peak in early spring (September, but without as high evaporation as in March). Evaporation decreases again to a secondary minimum in the summer (December). This is a similar annual pattern as in the entire Arctic Ocean (Taylor et al., 2018), although subregions in the Arctic Ocean behave differently.

In the Southern Ocean, the ice-free regime has the largest magnitude of positive evaporation, followed by the marginal ice regime, with negative evaporation in all but the spring months, and lastly the sea ice regime, with negative evaporation throughout the entire year. The evaporation from the ice-free ocean regime (Figure 3a, red line), unlike the entire ocean regime, has its largest evaporation in September, followed by a secondary smaller peak in March, and a minimum in December. The marginal ice and the sea ice regimes (Figure 3a, orange and blue lines) behave somewhat similarly, where evaporation is negative the majority of

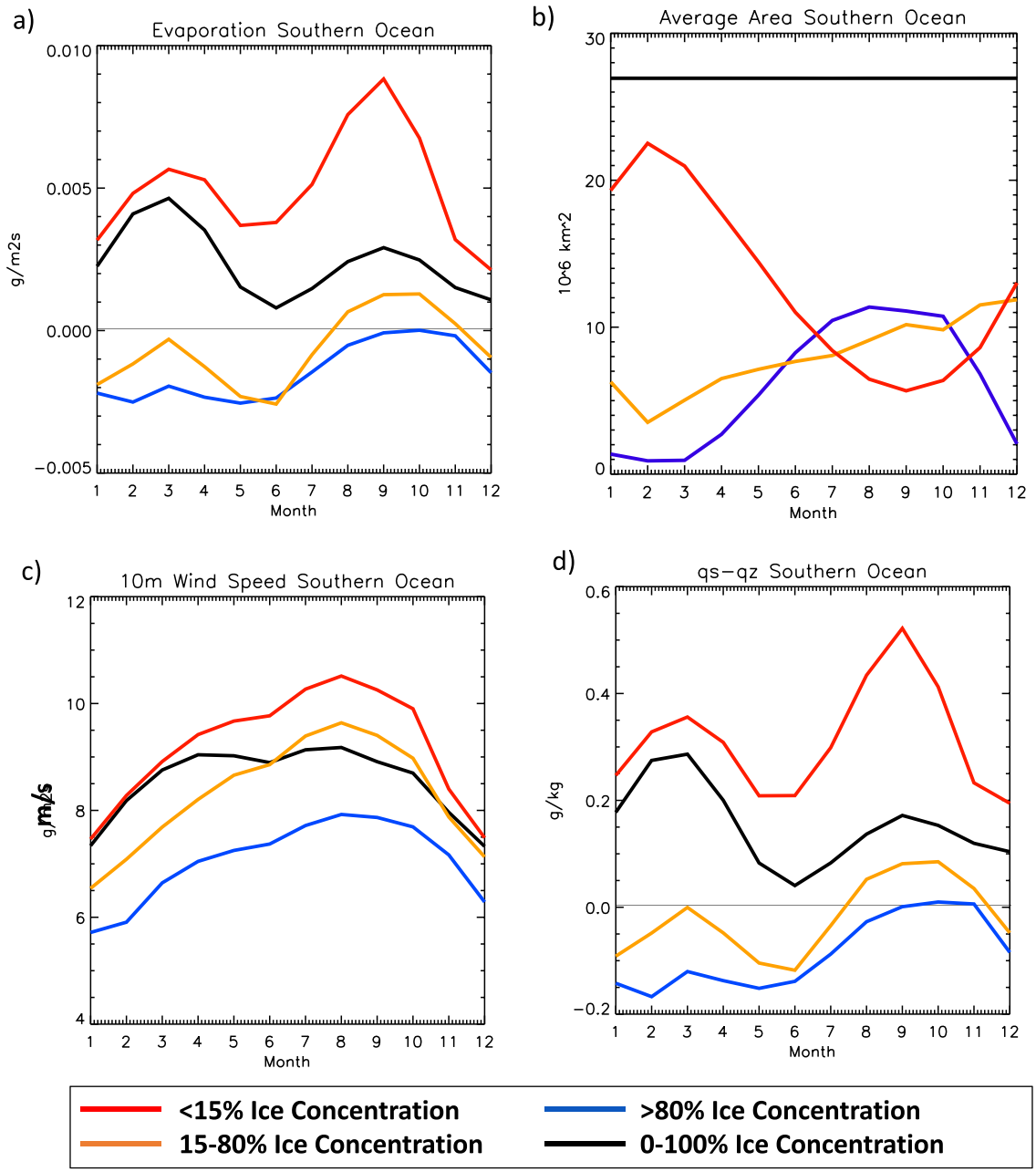

Figure 3. Climatological seasonal cycle 2003–2016 of (a) evaporation ($g \cdot m^{-2} \cdot s^{-1}$), (b) sea ice area for each sea ice regime (km^2), (c) 10-m wind speed (m/s), and (d) difference in specific humidity between the surface and atmosphere (g/kg) for the Southern Ocean. The Southern Ocean is split into different sea ice regimes: ice-free ocean (<15% ice concentration) in red, the marginal sea ice (15–80% ice concentration) in orange, the sea ice pack (>80% ice concentration) in blue, and the entire ocean regime (0–100% ice concentration) in black. Only the values in the sea ice mask (Figure 1a) are used for the monthly averages.

the year, peaks occurring in September–October (slightly positive or least negative), following a minimum evaporation in June (marginal ice regime) and May and February (sea ice regime). Although evaporation is very large over the ice-free ocean regime in September, it does not translate into the largest amount of evaporation overall. This is because the sea ice area reaches its maximum in September (Figure 3b, orange and blue lines) and the ice-free ocean regime reaches it minimum area (Figure 3b, red line) and covers most of the Southern Ocean in our sea ice mask (Figure 1a), thus dominating and dampening the evaporation signal significantly. The evaporation maximum in March is largely controlled by evaporation from the ice-free ocean regime, which reaches its maximum area at this time (Figure 3b, red line).

Table 3
Annual and Seasonal Evaporation Averages, Standard Deviations, and Trends for the Southern Ocean and Antarctic Seas Partitioned in Figure 1a for 2003–2016

	Southern Ocean	Weddell Sea	Indian Ocean	Pacific Ocean	Ross Sea	Bellingshausen/Amund Seas
			Mean $\overline{E}$ (Standard deviation)			
DJF	2.3 (1.3)	1.7 (1.5)	3.5 (1.7)	2.7 (1.3)	1.9 (1.5)	3.8 (1.7)
December	0.9 (0.8)	0.14 (0.8)	1.7 (1.5)	1.2(1.0)	0.6 (0.8)	2.2 (1.4)
MAM	3.1 (1.5)	2.9 (1.7)	5.9 (1.6)	3.5 (1.8)	1.5 (2.0)	3.4 (2.4)
March	4.6 (0.6)	4.0 (1.3)	6.8 (1.0)	5.1 (0.9)	4.3(1.9)	4.9 (1.8)
JJA	1.6 (0.87)	1.3 (1.2)	3.8 (1.3)	1.8 (1.4)	−0.23 (1.0)	2.7 (1.7)
June	0.6 (0.7)	0.4 (1.1)	3.1 (1.5)	0.5(1.0)	−1.3 (1.3)	1.3 (1.7)
SON	2.5 (1.0)	1.9 (1.1)	3.3 (1.5)	3.5 (1.7)	1.5 (1.0)	4.7 (1.7)
September	2.5 (0.7)	1.9 (0.8)	4.2 (1.0)	3.6 (2.1)	1.4 (1.0)	4.3 (1.7)
Yearly	2.2 (1.3)	1.7 (1.5)	3.8 (1.8)	2.7 (1.7)	1.1 (1.6)	3.6 (2.0)
			Trends $\delta\overline{E}$			
DJF	−0.056	−0.075	−0.084	−0.0064	−0.011	−0.11
December	−0.13	−0.16	−0.14	−0.063	−0.11	−0.17
MAM	−0.14	−0.20	−0.11	−0.12	−0.12	−0.15
March	−0.093	−0.17	−0.053	−0.095	−0.055	−0.028
JJA	−0.057	−0.067	−0.049	−0.097	−0.022	−0.098
June	−0.094	−0.18	−0.11	−0.079	−0.036	−0.084
SON	−0.094	−0.074	−0.095	−0.18	−0.092	−0.13
September	−0.026	−0.017	−0.029	−0.039	−0.009	−0.096
Yearly	−0.087	−0.10	−0.087	−0.10	−0.058	−0.12

Note. Extreme evaporation months during each season: December, March, June, and September are also included. Averages, standard deviations and trends are given in $\times 10^{-3}$ g · m^{-2} · s^{-1}. Trends that are statistically significant at the 95th percentile based on a simple Student's *t* test are shown in bold. Only values for the areas in the sea ice mask (colored areas shown in Figure 1a.) are included in the values.
Abbreviations: DJF: December-January-February; JJA: June-July-August; MAM: March-April-May; SON: September-October-November.

At the end of the melt season in February, the sea ice reaches its lowest area in the entire ocean regime (Figure 3b), followed by the largest differences in magnitudes between the specific humidity of the surface (q_s) and that of the overlying air (q_z) (q_s-q_z) (Figure 3d, black line) and the largest amount of evaporation in March. Since the entire ocean is dominated by the ice-free regime in March (Figure 3b), which has a positive evaporation rate, the evaporation for the Southern Ocean peaks. Although the ice-free ocean has a peak in evaporation in September (Figure 3a, red line), the entire ocean evaporation (Figure 3a, black line) is not as large as it is during March. This is because during September the ice-free ocean (red line) covers the smallest area and the sea ice regimes (orange and blue lines) cover the largest area (Figure 3b); thus, the sea ice regimes dominate the Southern Ocean evaporative flux (Figure 3a), and although the evaporation is positive in the sea ice regimes, it dominates the signal, creating a smaller positive flux compared to March. During December-January-February (DJF) when the ice-free ocean area dominates (Figure 3b, red line), this is also the time when the ocean surface has reached a similar temperature to that of the overlying air and the specific humidity between the ocean surface and the area is similar, wind speeds are low, and thus, the magnitude of evaporation is also low (Figure 3). Also, during these summer months when the entire ocean regime is mostly ice-free (Figure 3b), solar insolation warms the ocean surface. Since the heat capacity of the ocean is much larger than that of the overlying air, the air cools much faster than the ocean surface going into the fall. At this time, large differences in temperature and specific humidity of the surface and air occur (Figure 3d). This scenario creates positive evaporation and lines up with the evaporative flux maximum after the melt season in the entire ocean regime (March). This is also apparent in the sea ice and marginal ice regimes where the same scenario occurs over openings in the sea ice pack.

Throughout March-April-May (MAM), evaporation decreases rapidly in the entire ocean regime, corresponding to q_s approaching similar magnitude to q_z (Figure 3d). This is caused by the growth and consolidation of the sea ice pack during this time (Figure 3b), which restricts the exchange of moisture between the ocean and atmosphere and ice-free ocean temperatures begin to cool. In June-July-August (JJA), q_s and q_z are often similar in magnitude (Figure 3d) because the sea ice is growing back (Figure 3b, orange and blue lines), and the ice-free ocean is beginning to cool bringing the specific humidity of the surface similar to that of the overlying air. Also, during this season, the boundary layer is very stable, keeping the magnitude of

evaporation low, resulting in an average of 1.6×10^{-3} g · m^{-2} · s^{-1} (Figure 3a). Positive spikes in evaporation will still occur in the winter months over leads and polynyas (discussed later).

The sea ice area continues to increase and reaches it maximum extent in September in the entire ocean regime (Figure 3b), concurrent with the maxima of evaporation in the sea and marginal ice regimes. This seems counterintuitive; however, it is important to keep in mind that in both the marginal and sea ice regimes, areas where there are openings in the sea ice pack, the evaporation can be quite large and positive. This large evaporation is likely due to the occurrence of mesoscale coastal polynyas, which form above all during the spring months (Glorsen et al., 1992) along with strong winds (Figure 3c). These winds are likely cold and dry, either coming off of the Antarctic continent or blowing over the sea ice pack. When they come into contact with these openings in the sea ice pack, higher rates of evaporation occur caused by the large differences in specific humidity because the air is so cold and dry, and the ocean surface is near the freezing point. In the Southern Ocean the sea ice tends to drift, and the concentration fluctuates, and this, along with changing atmospheric conditions, can cause the fluxes of moisture to change from positive to negative quite frequently, depending on the conditions present compared to over the consolidated sea ice pack. Thus, the averaged flux over 14 years in these regimes are near zero or slightly negative (Figure 3a, yellow and blue lines), whereas on a day-to-day basis evaporation (positive flux) may often occur. In the late spring to summer (October–December) in the entire ocean regime, q_s-q_z decreases (Figure 3d), indicating that q_z increases faster than q_s. This is probably due to the faster warming of the air than the ocean, which has a large heat capacity. The decrease of q_s-q_z results in decrease of evaporation (Figure 3a).

The evaporation from the different regions of the Southern Ocean follows similar annual cycles to that of the entire Southern Ocean. This is evident from Figure 4 where these regions are split into the different oceanic regions from Figure 1. Like the entire Southern Ocean, each region has peaks in the evaporation around March and September, except for the Bellingshausen/Amundsen seas region where the magnitudes of evaporation during these months are roughly equal (Figure 4a). The wind speed in each region peaks in the spring, with a secondary peak around April (Figure 4c), and these combined with the largest specific humidity differences (Figure 4d) are what is driving and forming the dominant patterns of the seasonal evaporation cycle. The evaporation from the Indian Ocean is always the largest, followed by the Bellingshausen/Amundsen seas, with the Ross Sea having the smallest evaporation (Figure 4a). In all regions the evaporation remains on average positive throughout the year (Figure 4a), meaning that overall, the specific humidity of the air tends to be greater than the specific humidity of the ice (Figure 4d), except for the Ross Sea, having negative evaporation during the winter months.

The Ross Sea has the smallest monthly evaporation out of all the regions and even has a negative evaporative flux in May, June, and July, with an average of -9.0×10^{-4} g · m^{-2} · s^{-1} in June. This low evaporation is driven by the smallest difference in q_s-q_z (Figure 4d). The Indian Ocean sector has the largest evaporation between March and August with 6.9×10^{-3} g · m^{-2} · s^{-1} in March (blue line, Figure 4a). This corresponds with high wind speeds (Figure 4c), and a large difference in specific humidity (Figure 4d) and low sea ice concentration in March (Figure 4b). The Bellingshausen/Amundsen seas have the least amount of sea ice concentration year-round and one of the highest annual evaporation at 3.8×10^{-3} g · m^{-2} · s^{-1} (Figure 4a, red line) and is the only region where the evaporation cycle behaves slightly differently than the other regions. In this region, evaporation reaches two maxima that are nearly equal in magnitude in February and September and reaches its minimum in May, a month earlier than the other regions. This could be caused by a later return and increase in the sea ice concentration by 1 month compared to the other regions (Figure 4b). The second peak in September is due to a peak in the wind speed, a slight decrease in ice concentration, and a slight increase in the q_s-q_z (Figure 4).

6. Seasonal Evaporation From the Southern Ocean

The average seasonal spatial distributions (Figure 5a) again demonstrate that the location and concentration of the sea ice pack (Figure 5b) influence the direction of the evaporative flux. In winter (JJA) when the sea ice concentration and extent reach their maxima, the flux is generally from the atmosphere to the surface (negative) over the sea ice pack and from the ocean to the atmosphere (positive) over the ice-free ocean. In the sea ice and marginal ice regimes, the fluxes are very small and positive due to the less consolidated sea ice pack and larger occurrence of leads and open water. In spring (September-October-November

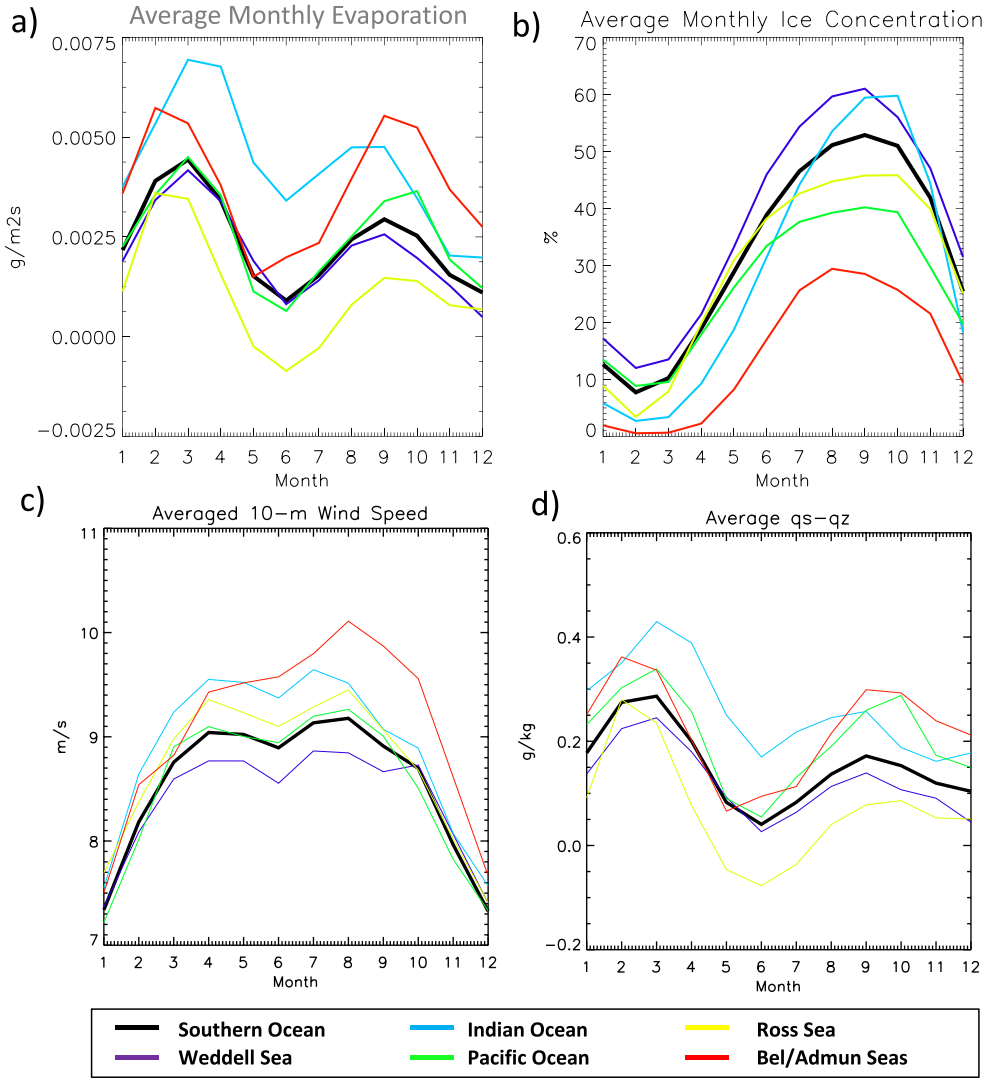

Figure 4. Average 2003–2016 monthly (a) evaporation, (b) sea ice concentration, (c) 10-m wind speed, and (d) difference in specific humidity from the surface and atmosphere for the five regional seas shown in Figure 1a. Only the values in the sea ice mask (Figure 1a) are used for the monthly averages.

[SON]), when the sea ice pack begins to break up and there is more ice-free ocean (leads and polynyas) mixed in with the sea ice pack, the average evaporation is close to zero, albeit slightly negative. In the summer months (DJF) when the majority of the sea ice pack has melted away, evaporation is generally near zero if not slightly positive due to the similar or slightly larger specific humidity of the ocean surface than the atmosphere. Areas where sea ice still persists (negative evaporation regions, light red) on average have a slight negative flux because the specific humidity of the air is sufficiently higher than the saturation specific humidity of the sea ice/snow surface during the summer. In fall (MAM) when the sea ice is beginning to grow back, the air is cooling at a faster rate (due to the heat capacity) than the ocean surface and fluxes from the ocean to the atmosphere are positive and large.

What is most noticeable from Figure 5 is a positive evaporative flux that is present in the summer and to a lesser extent, during the spring, fall, and winter months, in the Ross Sea adjacent to the Ross Ice Shelf. This area has a relatively shallow continental shelf, which has warm oceanic upwelling and inflow into the area throughout the year (Jacobs & Comiso, 1989), which causes the sea ice in this area to melt away completely in the summer months. The sea ice drift in this region is also divergent, forced by the cyclonic ocean circulation and causes formation of open water in front of the ice shelf throughout the year (Glorsen et al., 1992).

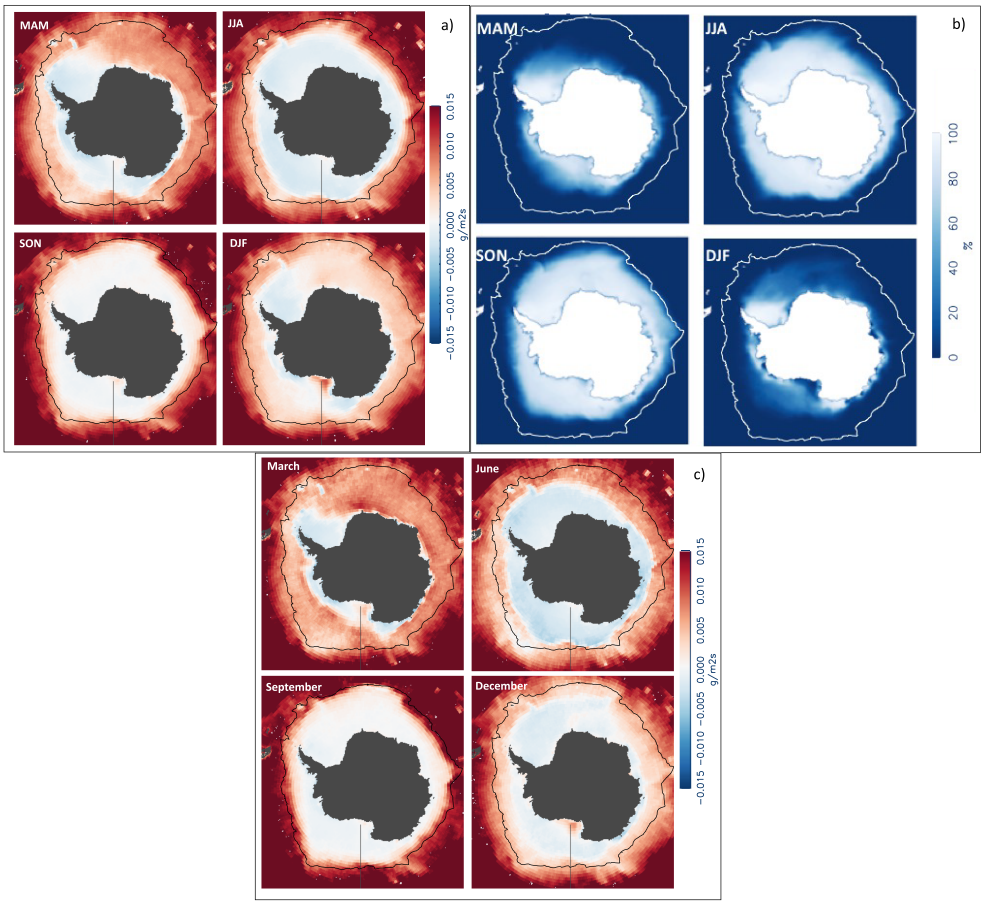

Figure 5. (a) Average (2003–2016) seasonal evaporation spatial maps of the Southern Ocean. Positive fluxes are from the surface to the atmosphere. The black line is the sea ice mask from Figure 1a. (b) Average (2003–2016) seasonal sea ice concentration maps of the Southern Ocean. The white line is the sea ice mask from Figure 1a. (c) Average (2003–2016) extreme-month (March, June, September, and December, respectively) evaporation maps for the Southern Ocean. Positive fluxes are from the surface to the atmosphere. The black line is the sea ice mask from Figure 1a.

Another mechanism that is occurring in this region is the presence of strong katabatic winds that blow down the ice sheet and into Terra Nova Bay and across the Ross ice shelf (Bromwich, 1989; Kurtz & Bromwich, 1985). These katabatic winds are cold and very dry, and thus, as they flow over these areas of open water, the large difference between the surface-specific humidity and that of the dry air creates strong evaporation. The added presence of openings in the sea ice pack and warmer ice-free ocean surface can facilitate an increase in evaporation from the ocean to the atmosphere, which is evident in the Ross Sea during all seasons in Figure 5.

Four months representing the extreme maximum (March and September) and minimum (June and December) evaporation are also shown in Figure 5c, and the averages and standard deviations are also included in Table 3. Compared to the seasonal averages, these monthly evaporation distributions produce similar spatial patterns in evaporation. The June and December (March and September) always have smaller (larger) average magnitudes of evaporation compared to the seasonal averages for the entire Southern Ocean as well as each regional sea, except for the Bellingshausen/Amundsen seas in September (Table 3). Since the minimum (maximum) sea ice extent occurs in March (September), the evaporation over the ice-free(-covered) ocean is higher (lower) than the seasonal average (Figure 5 and Table 3). In March, the magnitude of negative evaporation is larger over the sea ice pack in the Weddell, Ross, and Bellingshausen/Amundsen seas, but elsewhere the magnitude of the positive evaporation is larger. In September, the evaporation from the ice-free Southern Ocean regions are larger compared to the SON average. During June, evaporation is more negative over the sea ice pack and positive evaporation is smaller

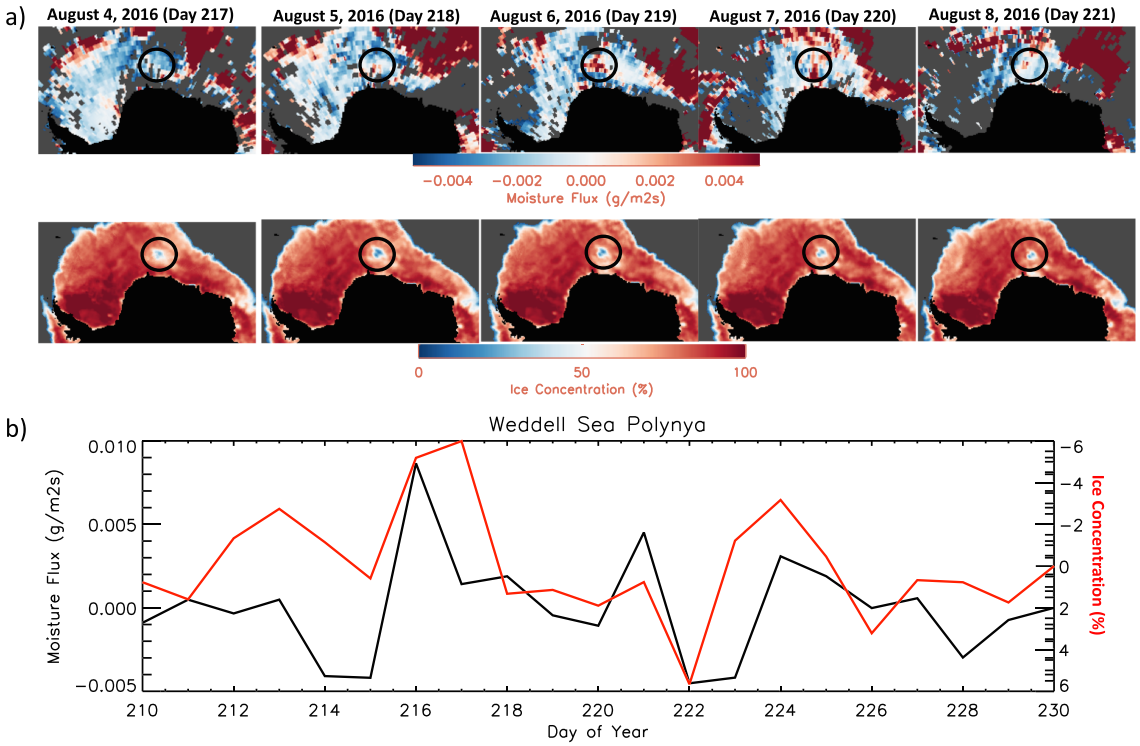

Figure 6. The 2016 Weddell Polynya. (a) Evaporation ($g \cdot m^{-2} \cdot s^{-1}$) from the Weddell Sea for 4–8 August 2016 (top row). Sea ice concentration for 4–8 August 2016 (bottom row). (b) The change in the evaporation (black) and the sea ice concentration (red) for the area in the black circle in (a) from the previous day minus the current day. Please note that the sea ice concentration axis is reversed to allow for ease of comparisons.

compared to the seasonal JJA average. In the beginning of summer (December), the evaporation is more negative over the Southern Ocean because although the air has warmed, the surface warms slower than the air; thus, the flux is mostly from the surface to the atmosphere. In January and February, the surface has warmed and the air begins to cool, so q_s and q_z are similar in magnitude over the sea ice, whereas the magnitude of q_s and q_z is larger over the ice free-ocean in December.

7. Weddell Polynya Study—4–8 August 2016

A polynya is a persistent or recurring opening in the sea ice pack that occurs in locations or climatological times when sea ice is otherwise normally present (Smith et al., 1990). Polynyas play an important role in the surface energy budget due to the large loss of heat and moisture from them, and the global ocean overturning circulation for their production of dense saline waters due to sea ice formation and brine rejection (Barber & Massom, 2007; Ohshima et al., 2013). Coastal polynyas, like the Ross Sea Polynya, often form around the Antarctic continent due to persistent winds blowing from the ice sheet over the sea ice pack, thus forcing the ice away from the shelf (Zwally et al., 1985). Other polynyas, such as the Weddell Polynya, occasionally form elsewhere in the sea ice pack.

The Weddell Polynya (also known as the Maud Rise Polynya) was a regular occurrence in the late 1970s (Parkinson, 1983) when continuous monitoring of the sea ice concentration began, but since these first few occurrences, this large polynya has not resurfaced until August 2016 and 2017. Conducting a case study of the 2016 Weddell Polynya allows for a better understanding of how evaporation behaves in association with polynyas. Figure 6a shows the evaporation (upper row) and sea ice concentration (lower row) from 4 to 8 August 2016. These dates were chosen because this was when the polynya was the largest in area and also had the lowest ice concentration during the month of August. From Figure 6a it is clear that as the polynya opens up (sea ice concentration decreases), the evaporative flux changes from negative (toward the surface) to positive (away from the surface) specifically in the region of the lower ice concentration in the polynya (black circles in Figure 6a). It is also interesting to note that as the ice concentration fluctuates

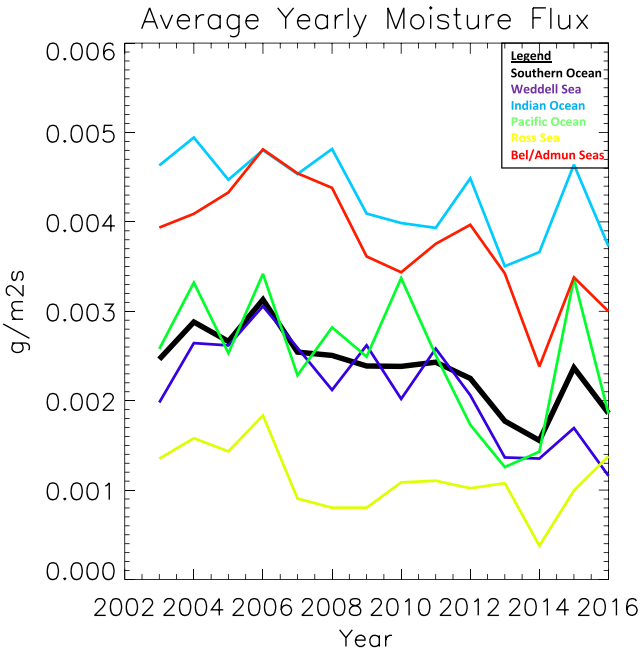

Figure 7. Yearly average time series of evaporation from the Southern Ocean and partitioned to the various seas outlined in Figure 1a. Only values from the sea ice mask (black line in Figure 1a.) are used.

throughout the polynya lifetime, the evaporation also fluctuates in conjunction. This is shown on the time series graph in Figure 6b where the ice concentration changes from 1 day to the next is shown with the respective change in evaporation. As the polynya loses (gains) sea ice concentration from 1 day to the next, the evaporation increases (decreases). The magnitude of the evaporative flux only correlates slightly (r=−0.55) with the sea ice concentration, again demonstrating that not only the sea ice cover but also the local weather effects (winds and air masses) can drastically alter the magnitude of the fluxes.

As the polynya forms, the relatively warm ocean surface is exposed to the cold, dry winter air, allowing for a large evaporation in a region, where only small fluxes (often condensation from air to ice) were previously occurring. During the lifetime of the 2016 Weddell Polynya, 0.012 g · m $^{-2}$ · s^{-1} of water (equivalent to 31 W/m^2 of latent heat) was evaporated to the atmosphere. Analogous studies have shown similar interactions occurring in the North Water Polynya in the Arctic (Boisvert et al., 2012). The excess moisture input to the atmosphere during these events usually creates low clouds or fog, which alter the surface energy budget.

8. Southern Ocean Evaporation Trends

The average annual evaporation in the Southern Ocean is 2.2×10^{-3} g · m $^{-2}$ · s^{-1} (6.0 W/m^2) and experiences significant interannual variability during 2003–2016 (black line, Figure 7), having a standard deviation of ~50% (1.3×10^{-3} g · m^{-2} · s^{-1} or 3.3 W/m^2) of the annual average (Table 3). Although there is variability, the overall trend is a decreasing one and statistically significant at the 95th percentile. Between 2003 and 2016, the average evaporation has decreased by ~1.1×10^{-3} g · m $^{-2}$ · s^{-1} (~2.8 W/m^2) or 52% compared to the 2003–2016 average (Table 3). The different regions in the Southern Ocean also show similar behavior, with large internally variability, and statistically significant decreasing trends (Figure 7 and Table 3). The largest change in evaporation over the 2003–2016 period occurs in the Bellingshausen/Amundsen seas, and the smallest change occurs in the Ross Sea. The regions do not show the same interannual variability (Figure 7), alluding to the unique regional climates that differ around the Antarctic Continent.

Spatially, the annual trend of evaporation in the Southern Ocean during 2003–2016 (Figure 8) shows a slightly different story than the averaged time series in Figure 7. A clear increasing trend in the evaporation is apparent in parts of the Ross and Bellingshausen/Amundsen seas, mostly close to the continent. In these specific areas the average trend in the evaporation is 4.9×10^{-5} g · m^{-2} · s^{-1} per year (equivalent to 0.1 W/m^2) in the Ross Sea and 2.2×10^{-5} g · m^{-2} · s^{-1} per year (equivalent to 0.06 W/m^2) in the Bellingshausen/Amundsen seas (outlined in black in Figure 8 and Table 4). Farther away from the continent, the trends go from neutral to slightly negative. In the Pacific Ocean sector, near the coast, there are small areas of increasing trends, located in areas where coastal polynyas occur (Barber & Massom, 2007). Annual trends are near neutral/slightly positive in the Western Weddell Sea, and pockets of increasing trends are apparent in the Indian Ocean. Besides these areas of positive trends in the evaporation, the majority of the annual trends are near neutral to negative (Table 3).

Annual trends in evaporation in the Southern Ocean are attributed to changing atmospheric and sea ice conditions between 2003 and 2016. Trends for the MERRA-2 10-m wind speed, specific humidity (q_s-q_z), and sea ice concentration are shown in Figure 9. From this figure it is clear that the trends in these variables are highly variable throughout the Southern Ocean. Changes from year to year are influenced by interannual variability of the 10-m wind speed, ice concentration, and specific humidity, all variables which are used to compute the evaporation. Since the changes in the sea ice concentration cause changes in the surface temperature and hence the surface-specific humidity, hence changing the magnitude of (q_s-q_z), we can therefore attribute changes to evaporation to changes in (q_s-q_z) and in the 10-m wind speed. From Figure 9, it is clear that the changes in the wind speed and humidities are decoupled; we can then follow Gao et al. (2013) to

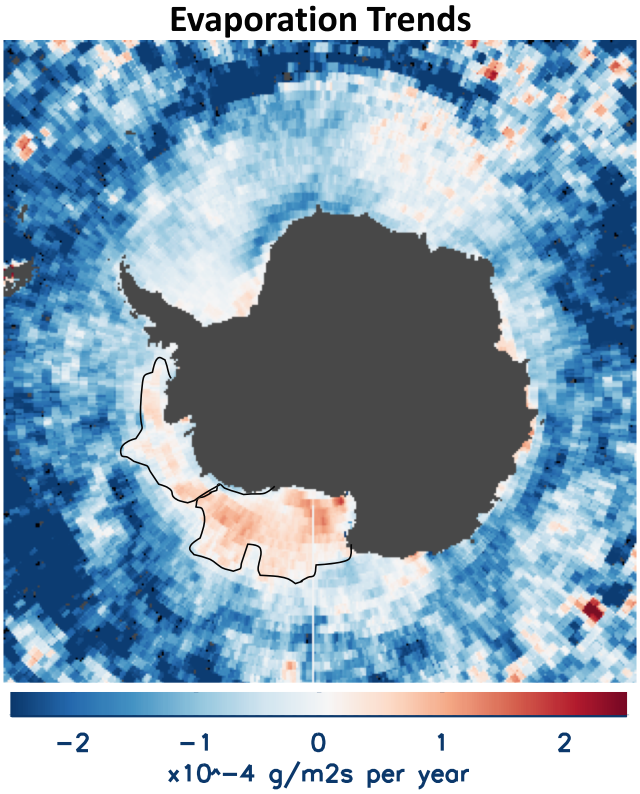

Figure 8. Annual trends in the Southern Ocean evaporation between 2003 and 2016. The black line outlines two additional (in the Bellingshausen/Amundsen and Ross seas) where additional average trends are calculated and discussed.

determine the contribution of each of these variables to the change in evaporation between 2003 and 2016. Specifically, (1) can be integrated to get (3) by ignoring any changes made in the transfer coefficient:

$$\frac{\delta\overline{E}}{\overline{E}} \approx \frac{\delta\overline{U}}{\overline{U}} + \frac{\delta\overline{Q}}{\overline{Q}} \tag{3}$$

where $\delta\overline{Q} = \delta\overline{q_s} - \delta\overline{q_z}$ is the specific humidity, U is the wind speed, $\delta\overline{x}$ is the change in the variable x, and $\frac{\delta\overline{x}}{\overline{x}}$ is the fractional change (i.e., the trend) of each variable. The overbar $\overline{x}$ specifies either the annual or seasonal average of each variable between 2003 and 2016 for the entire Southern Ocean, or each region shown in Figure 1a. Table 5 lists the change in $\overline{E}$, $\overline{Q}$,and $\overline{U}$, the percent change of each variable, along with the percent contribution of Q and U to changes in E between 2003 and 2016.

Table 5 shows that on average, evaporation in the Southern Ocean on an annual basis is decreasing at a rate of 4.0% between 2003 and 2016. This is driven by ~4% decrease in the magnitude of (q_s-q_z), in that the specific humidity of the air and the surface are becoming more similar. Ten-meter wind speeds on the other hand are only slightly increasing. Specifically, changes in (q_s-q_z) account for 97.5% and changes in the wind speed account for an opposite 2.0% to the changes in evaporation annual in the Southern Ocean (Table 5 and Figure 10). Annually, evaporation is decreasing in all regions between 2.3 and 5.9%, and this change is attributed mostly to a decrease in specific humidity difference and is lessened by a slight increase in wind speed (Table 5). This is the case for all regions except the Ross Sea and Pacific Ocean regions where there is a slight decrease in wind speeds as well.

The slight increases in wind speeds somewhat compensate the effects of the larger decrease in (q_s-q_z) on changes to evaporation. Specifically, in the Bellingshausen/Amundsen seas, the decrease in specific humidity accounts for 105% of the change in evaporation, which is compensated by a 2.6% increase in the wind speed (Table 5). Table 4 also shows occasions when the contribution changes in (q_s-q_z) and wind speeds do not equal to 100%, or the total change in evaporation. This is because other variables in (1) and their changes between 2003 and 2016, such as the air density and transfer coefficients, may also play a small role in the change in evaporation but are not accounted for in this particular assessment.

Increasing evaporation in the Ross Sea (Figure 8) is likely caused by a decrease in sea ice concentration just off the Ross ice shelf, which in turn causes increases in skin temperatures as more of the warmer ocean surface is exposed to the air (Figures 9b and 9c). The increase of evaporation in this area is driven mostly by the

Table 4
Average Increases in Evaporation Both Annually and Seasonally Between 2003 and 2016

Time Period	Ross Sea	Bellingshausen/Amundsen seas	Indian Ocean
Annual	4.9 (2.6%)	2.2 (0.6%)	
MAM	4.7 (1.3%)		
JJA	5.7 (52%)	5.4 (0.2%)	
SON	5.0 (4%)	4.8 (1%)	7.6 (2.2%)
DJF	11 (5.5%)		

Note. Percent increases in evaporation are listed in parenthesis. The values listed here are discussed in the text and the areas where these trends are computed are outlined in black in Figures 8 and 10. Values are given in $\times 10^{-5}$ g · m^{-2} · s^{-1}.
Abbreviations: DJF: December-January-February; JJA: June-July-August; MAM: March-April-May; SON: September-October-November.

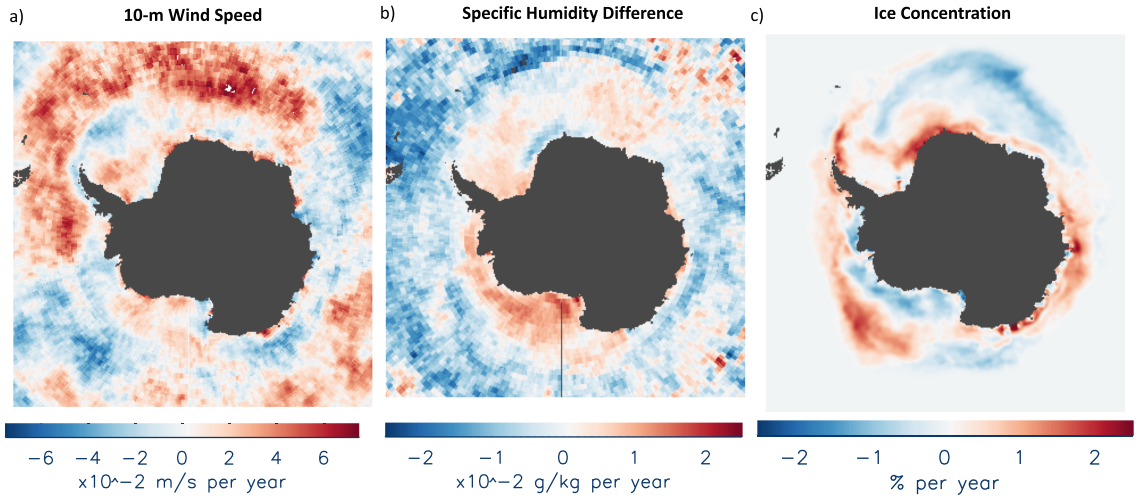

Figure 9. Annual (2003–2016) trends in (a) Modern-Era Retrospective Analysis for Research and Applications, Version 2 (MERRA-2) 10-m wind speed, (b) Atmospheric Infrared Sounder (AIRS) specific humidity difference (q_s-q_z), and (c) Special Sensor Microwave Imager (SSMI) sea ice concentration for the Southern Ocean.

increase in q_s-q_z and increases in wind speed (Figure 9). Loss of sea ice coverage and accompanied warmer surface temperatures and to a lesser extent stronger winds and drier air are causing the increased evaporation in this area. Conversely, there is a large decrease in evaporation just off the coast of Dronning Maud Land in the Weddell Sea (Figure 8). Here, an increase in sea ice concentration between 2003 and 2016 has caused a decrease in q_s-q_z; this decrease along with a slight increase in wind speeds has created a decrease in evaporation (Figure 9).

9. Seasonal Trends

Like the annual trends in evaporation in the Southern Ocean, seasonal trends on average are decreasing in all seasons and regions (Table 3). Decreasing trends are statistically significant in all regions in MAM, and in all regions except the Pacific Ocean in DJF, and in all regions except the Weddell and Ross seas and the Indian Ocean in SON. In JJA, all regions except the Pacific Ocean and Ross Sea produce statistically significant trends (Table 3). In each season there are specific areas where evaporation is, in fact, increasing, however (Figure 10). Similar to the annual trends, seasonal trends and interannual variability in the atmospheric and sea ice variables help to explain these changes. Seasonal trends of MERRA-2 10-m wind speed, specific humidity difference (q_s-q_z), and sea ice concentration are shown in Figure 11, and the percent contribution to variance of these variables in each season are listed in Table 5. Like with the annual changes, the variance in evaporation is largely driven by changes in the specific humidity differences and very slightly by changes in the wind speed.

In MAM, the average evaporation trend in the Southern Ocean is -1.4×10^{-4} g · m^{-2} · s^{-1} (Table 3; 4.5% decrease per year; Table 5) and on average, evaporation in each of the regions is decreasing between 1.9 and 8.0% per year (Table 5). Like in the annual trends, there are areas of the Southern Ocean where the evaporation trends are positive. The largest increases in evaporation during MAM are apparent in the Ross and Bellingshausen/Amundsen seas, where fluxes have increased 4.7×10^{-5} g · m^{-2} · s^{-1} per year since 2003 (or 1.3% per year; the areas where the trend is calculated are outlined with the black line in Figure 10a and Table 4). There has also been a slight increase in the Weddell Sea close to the peninsula, although the magnitude is smaller. In the Weddell Sea in general, the evaporation variance is largely driven by changes in the specific humidity difference (Table 5). In this area of increasing evaporation q_s-q_z is increasing slightly (Figure 11b), but this is not caused by a change in ice concentration (Figure 11c), so it appears that this increase in q_s-q_z is driven by more cold, dry air originating from the Antarctic continent over this area, lowering q_z, and hence increasing evaporation. Evaporation is decreasing nearly everywhere else, especially near the coast of East Antarctica (Figure 10a). In this area, increasing sea ice concentrations, which help

Table 5
The Average and Seasonal Evaporation (E) Trends and the Respective Contributions From the Specific Humidity Difference ($\overline{Q} = \overline{q_s} - \overline{q_z}$) and Wind Speed ($\overline{U}$) Between 2003 and 2016 in the Southern Ocean

Variable	Southern Ocean	Weddell Sea	Indian Ocean	Pacific Ocean	Ross Sea	Bellingshausen/Amund Seas
			Annual			
$\delta\overline{E}/\overline{E}$	−4.0%	−5.9%	−2.3%	−3.7%	−5.9%	−3.4%
$\overline{Q}$ (kg/kg)	0.14–5.6 × 10^{-3}	0.10–6.5 × 10^{-3}	0.24–5.6 × 10^{-3}	0.20–6.8 × 10^{-3}	0.06–3.7 × 10^{-3}	0.22–8.0 × 10^{-3}
$\delta\overline{Q}$ (kg/kg)	−3.9%	−6.5%	−2.3%	−3.4%	−6.6%	−3.6%
$\delta\overline{Q}/\overline{Q}$	97.5%	110%	100%	92%	112%	105%
$\delta\overline{Q}/\delta\overline{E}$						
$\overline{U}$ (m/s)	8.3	8.2 1.7 × 10^{-2}	8.5 7.8 × 10^{-3}	8.1–6.1 × 10^{-3}	8.6–2.3 × 10^{-3}	8.7
$\delta\overline{U}$ (m/s)	6.5 × 10^{-3}	0.2%	0.09%	−0.08%	−0.03%	0.01
$\delta\overline{U}/\overline{U}$	0.08%	−3.4%	−3.9%	2.2%	0.5%	0.1%
$\delta\overline{U}/\delta\overline{E}$	−2.0%					−2.6%
			MAM (Fall)			
$\delta\overline{E}/\overline{E}$	−4.5%	−7.0%	−1.9%	−3.4%	−8.0%	−4.4%
$\overline{Q}$ (kg/kg)	0.18–8.5 × 10^{-3}	0.16–1.2 × 10^{-2}	0.35–5.9 × 10^{-3}	0.23–7.4 × 10^{-3}	0.07–6.7 × 10^{-3}	0.20–9.4 × 10^{-3}
$\delta\overline{Q}$ (kg/kg)	−4.7%	−7.5%	−1.7%	−3.2%	−9.5%	−4.7%
$\delta\overline{Q}/\overline{Q}$	104%	107%	89.5%	94.1%	119%	107%
$\delta\overline{Q}/\delta\overline{E}$						
$\overline{U}$ (m/s)	8.6	8.5	9.0–6.4 × 10^{-3}–0.07%	8.6–7.1 × 10^{-3}–0.08%	8.9–2.7 × 10^{-3}	9.0
$\delta\overline{U}$ (m/s)	3.0 × 10^{-3}	0.01	3.7%	2.4%	−0.03%	8.8 × 10^{-3}
$\delta\overline{U}/\overline{U}$	0.03%	0.1%			0.4%	0.1%
$\delta\overline{U}/\delta\overline{E}$	−0.7%	−1.4%				−2.3%
			JJA (Winter)			
$\delta\overline{E}/\overline{E}$	−3.6%	−5.2%	−1.3%	−5.4%	−9.6%	−3.6%
$\overline{Q}$ (kg/kg)	0.09–2.9 × 10^{-3}	0.07–3.5 × 10^{-3}	0.21–2.4 × 10^{-3}	0.13–5.3 × 10^{-3}	−0.02	0.15–4.0 × 10^{-3}
$\delta\overline{Q}$ (kg/kg)	−3.2%	−5.0%	−1.1%	−4.1%	−1.1 × 10^{-3}	−2.6%
$\delta\overline{Q}/\overline{Q}$	88.9%	96.2%	84.6%	72%	−5.5%	72.2%
$\delta\overline{Q}/\delta\overline{E}$					57.3%	
$\overline{U}$ (m/s)	8.8	8.6 7.4 × 10^{-3}	9.1 3.2 × 10^{-3}	8.7–5.7 × 10^{-3}	9.1	9.5
$\delta\overline{U}$ (m/s)	−0.01	0.09%	0.04%	−0.07%	−0.05	−0.04
$\delta\overline{U}/\overline{U}$	−0.1%	−1.7%	−3.1%	1.3%	−0.6%	−0.4%
$\delta\overline{U}/\delta\overline{E}$	2.8%				6.3%	11.1%
			SON (Spring)			
$\delta\overline{E}/\overline{E}$	−3.8%	−3.9%	−2.9%	−5.1%	−6.1%	−2.8%
$\overline{Q}$ (kg/kg)	0.16–5.6 × 10^{-3}	0.12–5.0 × 10^{-3}	0.21–4.5 × 10^{-3}	0.25–0.01	0.08	0.29–8.4 × 10^{-3}
$\delta\overline{Q}$ (kg/kg)	−3.5%	−4.1%	−2.1%	−4.0%	−5.3 × 10^{-3}	−2.9%
$\delta\overline{Q}/\overline{Q}$	92.1%	105%	72.4%	78.4%	−6.6%	104%
$\delta\overline{Q}/\delta\overline{E}$					108%	
$\overline{U}$ (m/s)	8.4	8.4	8.5	8.2	8.6–4.5 × 10^{-3}	9.2
$\delta\overline{U}$(m/s)	2.0 × 10^{-3}	0.03	−0.02	−0.02	−0.05%	4.7 × 10^{-3}
$\delta\overline{U}/\overline{U}$	0.02%	0.4%	−0.2%	−0.3%	0.8%	0.05%
$\delta\overline{U}/\delta\overline{E}$	−0.5%	−10.2%	6.9%	4.7%		−1.8%
			DJF (Summer)			
$\delta\overline{E}/\overline{E}$	−2.4%	−4.4%	−2.4%	−0.2%	−0.6%	−2.9%
$\overline{Q}$ (kg/kg)	0.18–6.0 × 10^{-3}	0.12–6.6×10^{-3}	0.27	0.22–2.8 × 10^{-3}	0.13–2.3 × 10^{-3}	0.27
$\delta\overline{Q}$ (kg/kg)	−3.3%	−5.5%	−8.8 × 10^{-3}	−1.2%	−1.8%	−0.01
$\delta\overline{Q}/\overline{Q}$	137%	125%	−3.3%	600%	300%	−3.7%
$\delta\overline{Q}/\delta\overline{E}$			137%			128%
$\overline{U}$/ (m/s)	7.4	7.4	7.4	7.0	7.6	7.5
$\delta\overline{U}$/ (m/s)	0.04	0.02	0.06	0.02	0.05	0.05
$\delta\overline{U}/\overline{U}$	0.5%	0.3%	0.8%	0.2%	0.66%	0.7%
$\delta\overline{U}/\delta\overline{E}$	−20.8%	−6.8%	−33.3%	−100%	−110%	−24.1%

Note. The fractional change ($\delta\overline{x}$) for each variable and the percent change ($\delta\overline{x}/\overline{x}$) in the variable are also listed. Average annual and seasonal evaporation ($\overline{E}$) and the change in evaporation ($\delta\overline{E}$) are listed in Table 3. Finally, the percent contribution of $\overline{Q}$ and $\overline{U}$ to changes in $\overline{E}$ ($\delta\overline{x}/\delta\overline{E}$) are listed as percentages. Values are computed from Equation (3). Values of ($\delta\overline{x}/\overline{x}$) that bear a "−" (negative sign) play an "opposite" effect in the overall $\delta\overline{E}$. The regions and sea ice mask are used in these calculations and are highlighted in Figure 1a.
Abbreviations: DJF: December-January-February; JJA: June-July-August; MAM: March-April-May; SON: September-October-November.

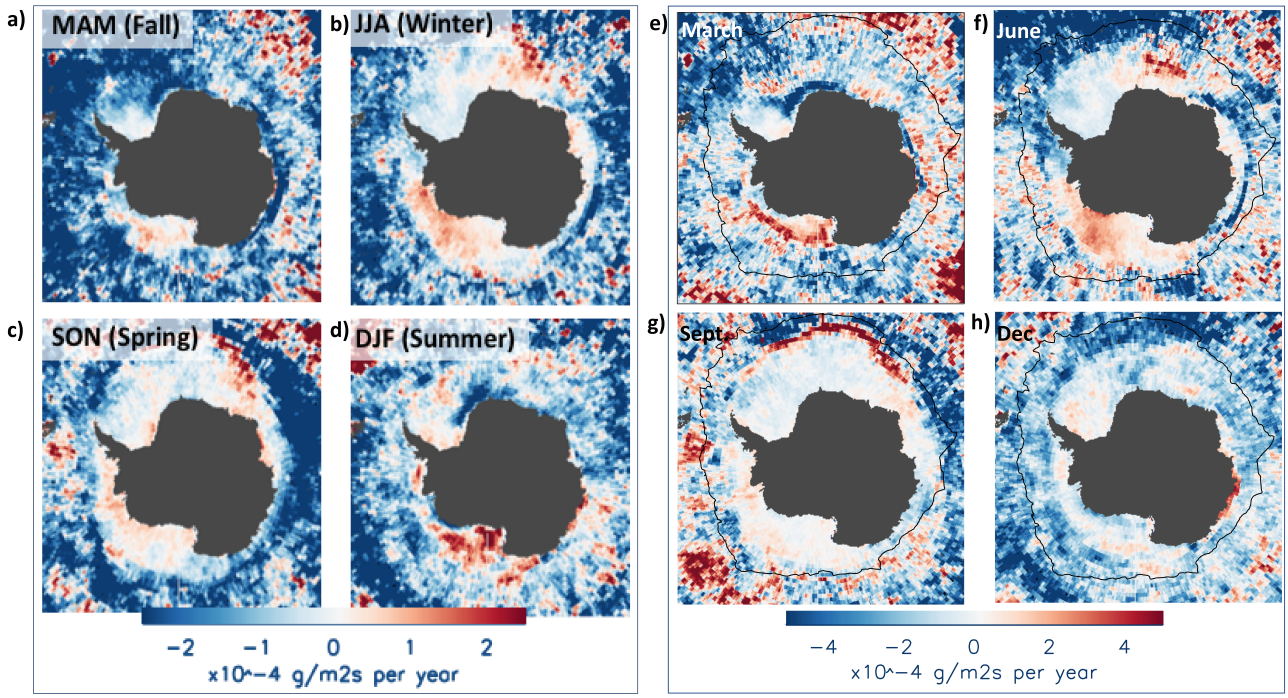

Figure 10. Seasonal spatial trends in Southern Ocean evaporation between 2003 and 2016 for (a) fall (March-April-May [MAM]), (b) winter (June-July-August [JJA]), (c) spring (September-October-November [SON]), and (d) summer (December-January-February [DJF]). The black line outlines areas where additional average trends are calculated and discussed in the text. Extreme monthly trends in the Southern Ocean evaporation between 2003 and 2016 for (e) March, (f) June, (g) September, and (h) December.

to cause a decrease in q_s-q_z, and decreasing wind speeds (Figure 11) are causing this marked decrease in evaporation. The variance in the evaporation for the Southern Ocean during MAM appears to be driven largely by the changes in q_s-q_z, while changes in the wind speed were negligible (Table 5).

In JJA, in areas of the sea ice mask, evaporation is increasing in the Bellingshausen/Amundsen and Ross seas and in small areas of the Indian Ocean (Figure 10b). Negative and near-neutral trends are occurring elsewhere. Evaporation is increasing in the Bellingshausen/Amundsen seas at 5.4×10^{-5} g · m^{-2} · s^{-1} per year (or 2% per year) and in the Ross Sea at 5.7×10^{-5} g · m^{-2} · s^{-1} per year (or 52%; see area outlined in black in Figure 10b and Table 4). In these regions, although the sea ice concentration is fairly constant during 2003–2016, and wind speeds have decreased in some areas and increased in others, q_s-q_z has increased slightly (Figure 11). The northward wind component and the air specific humidity are also negatively correlated here (Figure 12c), meaning that winds from the south (north) are correlated with drier (moister) air. Hence, this decrease in moisture in the air (Figure 11b) is likely driven by cold, dry air flowing off the Antarctic continent. As the sea ice concentration does not vary much in this area, the air humidity is the driving factor in the variance of the evaporation and is decreasing over the time period, causing the increase in q_s-q_z. Thus, this cold, dry air, having a lower specific humidity compared to that of the sea ice surface and leads, allows for an increase in evaporation from the surface to the atmosphere. Considering the regional averages of evaporation in JJA, decreasing trends dominate (Table 3) and like in MAM, are caused predominantly by a decrease in the specific humidity difference (Table 5).

Similar to JJA, in SON, the average evaporation in the Southern Ocean is decreasing at a rate of -9.5 $\times 10^{-5}$ g · m^{-2} · s^{-1} per year (3.8% per year; Figure 10c and Table 3). Areas where increasing evaporation has occurred in JJA are similar to SON; however, the magnitude in SON tends to be slightly less. This is apparent in the Bellingshausen/Amundsen and Ross seas, where evaporation is increasing at 4.8×10^{-5} g · m^{-2} · s^{-1} per year (1% per year) and 5.0×10^{-5} g · m^{-2} · s^{-1} per year (4% per year), respectively (areas outlined in Figure 10c in black, Table 4). Trends in the variables show decreasing sea ice concentration, increasing q_s-q_z and winds, which likely cause the changes in those regions (Figure 11). Unlike in JJA, the correlation between the

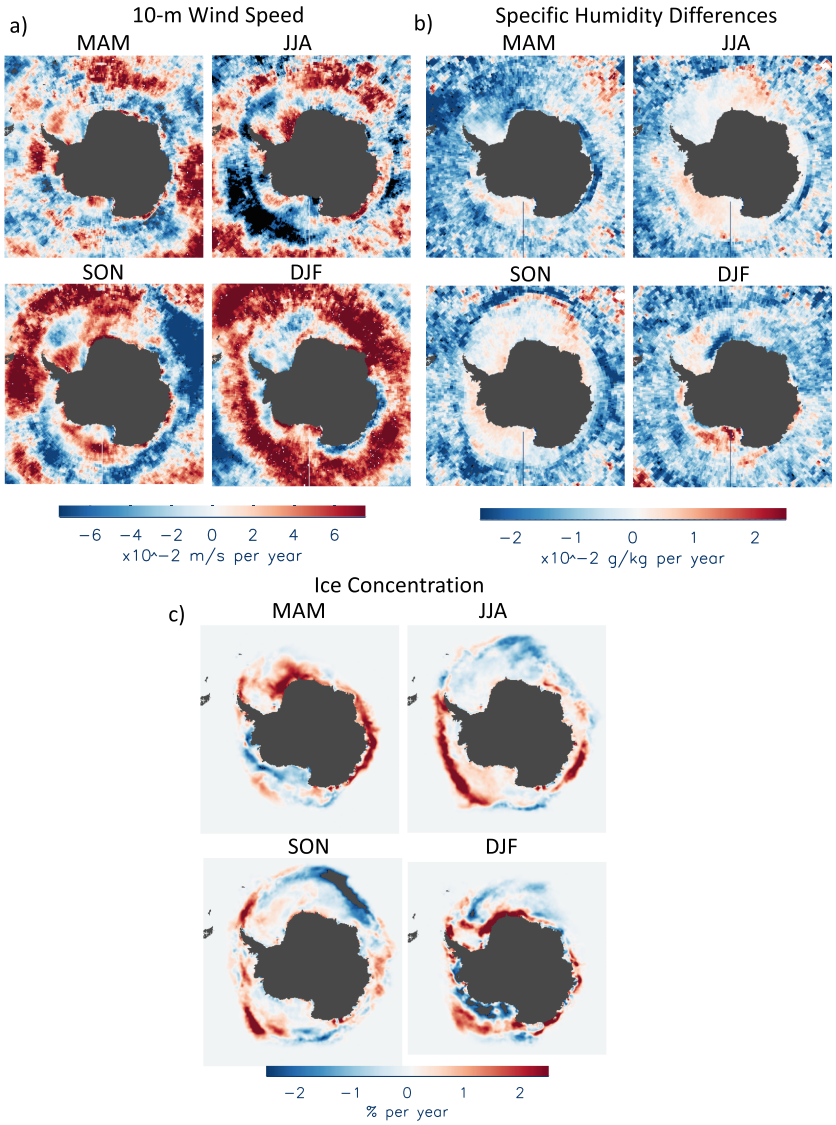

Figure 11. Seasonal spatial trends in the Southern Ocean (a) Modern-Era Retrospective Analysis for Research and Applications, Version 2 (MERRA-2) 10-m wind speeds, (b) Atmospheric Infrared Sounder (AIRS)-specific humidity difference (q_s-q_z), and (c) Special Sensor Microwave Imager (SSMI) sea ice concentration for 2003–2016.

northward wind component and the air specific humidity is neutral in SON, in that the direction of the winds does not dictate the humidity of the air (Figure 12d). The air masses might not be originating from the continent and are perhaps not as dry as those which likely originated there in JJA. This in turn has likely caused the trends in the evaporation to not be as large as in JJA.

The large increases in evaporation from the Indian Ocean sector (7.6×10^{-5} g · m^{-2} · s^{-1} [2.2% per year], outlined in black in Figure 10c and Table 4) in SON are occurring along the edge of the sea ice pack and are most likely responding to a large decrease in sea ice concentration and associated increase in surface specific humidity (Figures 11b and 11c). In this region of the Indian Ocean, changes in evaporation are driven by changes at the sea surface, driving increases in q_s-q_z rather than changes in the wind speed. Other evaporation trends within the sea ice mask during SON are near zero or slightly negative (Figure 10c).

Finally, in DJF, although the average trend in the Southern Ocean is negative (-5.6×10^{-5} g · m^{-2} · s^{-1} or 2.4% per year; Table 3), the largest positive trends compared to any season occur in the Ross Sea (Figure 10d). The Ross Sea has a 1.0×10^{-4} g · m^{-2} · s^{-1} (5.5%) per year increase or an accumulated increase of 1.3×10^{-3} g ·

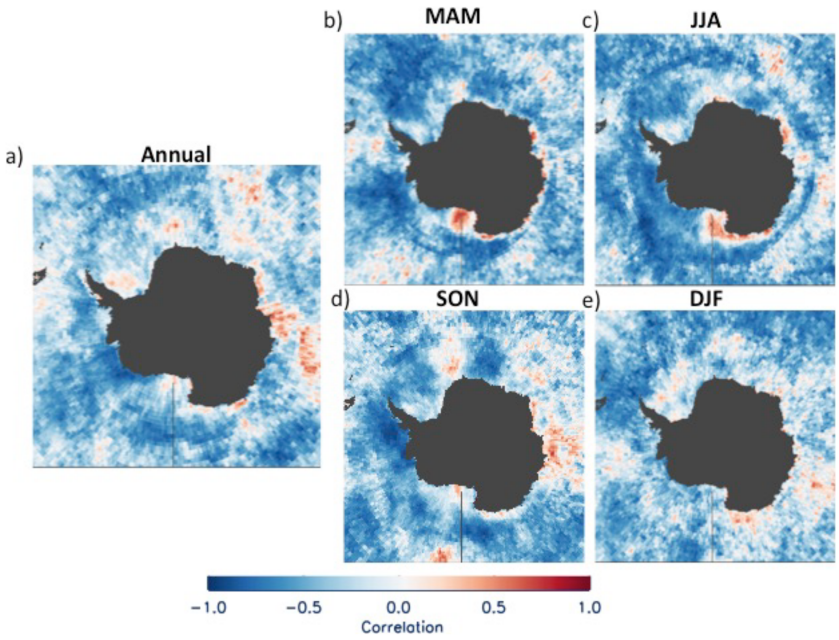

Figure 12. Correlations during 2003–2016 between the northward (v) 10-m Modern-Era Retrospective Analysis for Research and Applications, Version 2 (MERRA-2)wind component and the Atmospheric Infrared Sounder (AIRS)air specific humidity (q_z) for (a) annual, (b) fall (March-April-May [MAM]), (c) winter (June-July-August [JJA]), (d) spring (September-October-November [SON]), and (e) summer (December-January-February [DJF]).

$m^{-2} \cdot s^{-1}$ (equivalent to 3.3 W/m^2 in latent heat flux) since 2003 (area outlined in black in Figure 10d and Table 4). Some locations in the Ross Sea have seen a 2.5×10^{-4} $g \cdot m^{-2} \cdot s^{-1}$ per year increase, equivalent to 8.8 W/m^2 (or 14%) in latent heat flux. These increases are due to a loss in sea ice coverage (Figure 11a), warmer ocean temperatures, thus increasing the surface specific humidity, increasing q_s-q_z (Figure 11b). This combined with an increase in wind speeds (Figure 11a) have caused evaporation to increase in this area (Figure 10d). Increasing evaporation is also occurring in the Western Weddell Sea (Figure 10d) but is not driven by changes in sea ice concentration (Figure 11a) or the decreasing wind speeds (Figure 11c).

Pockets of increasing evaporation are also seen in the Pacific Ocean, the Bellingshausen/Amundsen seas, and the Indian Ocean in DJF (Figure 10d). These are mostly located near the coasts of Antarctica and, unlike in the Ross Sea, are largely driven by changes in q_s-q_z compared to changes in the winds because here they are decreasing (Figure 11). The evaporation is decreasing in all regions in DJF on average (Table 3); however, unlike the other seasons, the wind speed plays a slightly larger role (percentage) in the variance of the evaporation, but the change in the q_s-q_z still dominates the signal (Table 5).

From this analysis it is apparent that the cause of the variability of evaporation from the Southern Ocean depends on the season and region. For example, in the Ross Sea, the largest positive trends in the evaporation occur in JJA and DJF, and these changes are largely influenced by changes in the specific humidity difference (Figure 11), where during this time the specific humidity difference is increasing along with the winds (Figure 11b). In MAM and SON, the ice concentration and surface-specific humidity are the main drivers (Figure 11 and Table 5), as during these seasons the ice concentration is decreasing and q_s is increasing quicker than q_z, causing an increase in q_s-q_z in the Ross Sea (Figure 11).

When focusing on the trends in evaporation for the extreme maximum and minimum evaporation months (Figures 10e–10h), unlike the averages (Figure 5), the monthly trends are not always similar to the seasonal trends (Table 3). It is apparent, however, that the increasing evaporation in March (Figure 10e) and June (Figure 10f) in the Ross and Bellingshausen/Amundsen seas is driving the increased evaporation in MAM and JJA. Conversely, the trends in September and December in these same regions are not driving the increased seasonal evaporation, and it is likely that the other months during these seasons are responsible. The increasing evaporation in September along the sea ice edge in the Weddell Sea and Indian Ocean

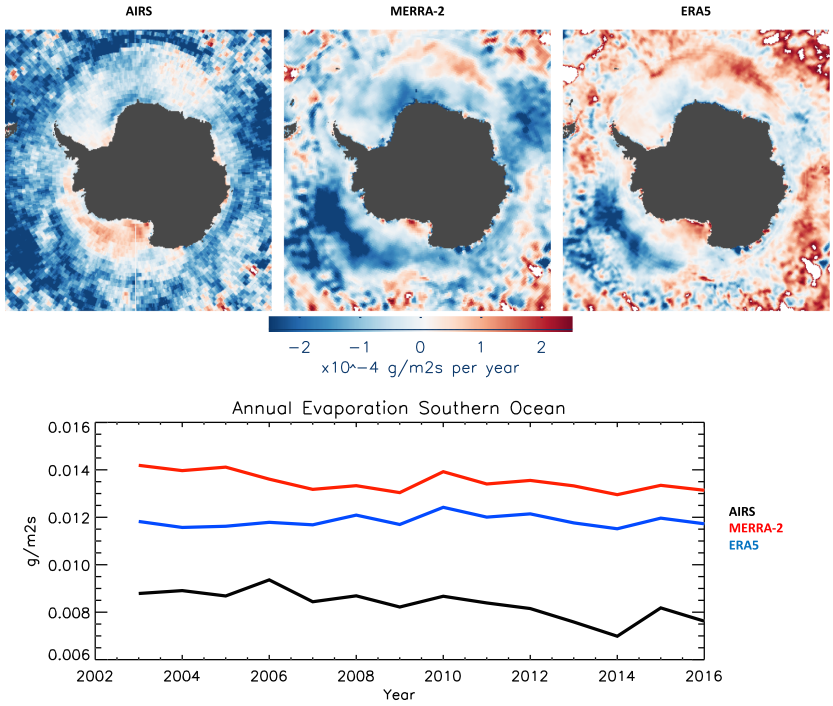

Figure 13. Top: Annual trends for 2003–2016 in evaporation from the (left) Atmospheric Infrared Sounder (AIRS)-derived product, (middle) Modern-Era Retrospective Analysis for Research and Applications, Version 2 (MERRA-2) , and (right) ERA5. Bottom: Average annual evaporation between 2003 and 2016 for the AIRS derived product (black), MERRA-2 (red), and ERA5 (blue).

appears to drive the increasing evaporation seen here in SON. The magnitudes of the trends in the extreme months are larger than those seasonally (Table 3).

10. Comparisons With MERRA-2 and ERA5 Evaporation

Trends and annual averages of evaporation are compared with two different reanalysis products in the Southern Ocean during 2003–2016. NASA MERRA-2 (Gelaro et al., 2017), and the recently released European Center for Medium-Range Weather Forecasts (ECMWF) ERA5 (Hersbach & Dee, 2016) reanalyses are used for this comparison. The annual trends and the average annual evaporation for each are shown in Figure 13, and it is clear that neither of the products agree completely. The magnitude of each product's evaporation differ, with MERRA-2 being the largest, ERA5 in the middle, and AIRS the lowest, with 1.4×10^{-2} g · m^{-2} · s^{-1}, 1.2×10^{-2} g · m^{-2} · s^{-1}, and 9.0×10^{-3} g · m^{-2} · s^{-1}, respectively. They also do not appear to follow the same interannual variability. MERRA-2 drops off slightly between 2003 and 2006, ERA5 remains fairly constant, and AIRS shows a decreasing trend. All products have an increase in evaporation in 2010, and MERRA-2 and ERA5 have similar interannual variability after that, but not before. The trends between the products also differ. For example, ERA5 has the most areas of increasing trends compared to MERRA-2 and AIRS, which have more similarities in spatial trends (Figure 13, top).

Regardless of this, all of the evaporation products show similar spatial increasing trends in the Ross Sea near the Ross Ice Shelf and in parts of the Bellingshausen/Amundsen seas, although the smallest trends occur in MERRA-2 (Figure 13, top). All three products also have positive trends in the Indian Ocean at 60S latitude, with AIRS having the smallest trend. Negative trends in the eastern Weddell Sea near Dronning Maud Land and in the Bellingshausen/Amundsen seas at lower latitudes are common in all three products. Although there are some similarities in the spatial trends between the three products, they are also not identical, highlighting the difficulty and uncertainty in estimating evaporation in the Southern Ocean. Further work needs to be undertaken to determine the root causes for the differences between the products, whether that be

differences in data assimilation, snow and sea ice schemes, surface flux and boundary layer parameterizations, or assumptions used in calculating the evaporation. However, this is out of the scope of this paper.

11. Conclusions

Daily evaporation from the Southern Ocean was estimated for the period 2003–2016 applying an updated turbulent flux algorithm, which uses as input satellite remote sensing data from AIRS (air specific humidity, skin temperature, and geopotential height), reanalysis wind speeds from MERRA-2, and sea ice concentration from SMMI. This novel approach has performed well in the Arctic Ocean (Boisvert et al., 2013), on the Greenland ice sheet (Boisvert et al., 2016), and now for the Southern Ocean. Three buoys deployed in the Weddell Sea in 2016 were used to assess the reliability of AIRS and MERRA-2 data used to calculate the evaporation. The temperature, humidity, and winds showed good overall agreement, where AIRS temperature and humidity had smaller biases than MERRA-2 when compared to the buoy data. An error estimate analysis on these variables revealed a 34% uncertainty in the evaporation product for the Southern Ocean. This analysis provided confidence in our results and analysis of evaporation from the Southern Ocean from AIRS data between 2003 and 2016.

This evaporation dataset has given considerable insight into the annual, seasonal, and regional similarities, differences, and changes that have taken place in the Southern Ocean in recent years.

1. In all regions but the Bellingshausen/Amundsen seas, the annual cycle of evaporation has a peak in March, directly after the sea ice minimum, followed by a minimum evaporative flux in June when the sea ice concentration is rapidly increasing. Another peak in evaporation, albeit smaller than in March, occurs in September around the time of the sea ice maximum and the evaporative flux decreases again as the sea ice begins to melt.
2. Evaporation from the marginal and sea ice regimes is largest in September, followed by March, although these magnitudes are negative or close to zero. The ice-free regime also has the largest evaporation in September, but encompasses a smaller area due to the sea ice maximum, and does not have a large effect on the area-averaged evaporation from the entire Southern Ocean. In March evaporation from the entire Southern Ocean is dominated by evaporation from the ice-free regime.
3. Annual evaporation shows considerable interannual variability, and decreased annual evaporation occurs throughout 2003–2016 over most of the Southern Ocean. The Indian Ocean sector had the largest annual trend, and the Ross Sea sector had the smallest trend.
4. Seasonal trends in evaporation during 2003–2016 are generally negative. However, increased evaporation occurred in parts of the Ross and Bellingshausen/Amundsen seas over the time period. Largest increasing trends occurred in the Ross Sea in JJA and DJF.
5. Overall, variations in the specific humidity difference (q_s-q_z) dominate the change in evaporation, with changes in the wind speed playing a smaller role on an annual, seasonal and regional basis. Changes in sea ice concentration and, hence, in surface specific humidity and q_s-q_z play a large role in the magnitude and interannual variance of fall, spring, and annual mean evaporation. In the winter and summer, the interannual variance in evaporation is largely controlled by the air specific humidity. Here the location where the winds originate from contributed to the changes in the specific humidity difference (q_s-q_z). Winds, altering the atmospheric humidity (either cold and dry air from the Antarctic continent or warm and moist air from the lower latitudes of the Southern Ocean), played a large role in the sign and magnitude of evaporation.
6. When comparing these annual and interannual results with evaporation products from MERRA-2 and ERA5, it was found that they exhibit some similar spatial patterns of trends, but the magnitudes of evaporation are quite different.
7. The results for seasonal mean evaporation can be compared against a few previous studies. In the Ice Station Weddell in fall-winter 1992 in the western Weddell Sea Andreas et al. (2004) observed predominantly near-zero evaporation. For the same region and period, ERA-Interim and ERA-40 reanalyses suggested slight condensation, whereas NCEP-Climate Forecast System Reanalysis (CFSR), NCEP-Department of Energy (DOE), and MERRA reanalyses suggested weak evaporation (Tastula et al., 2013). Our results suggested slight condensation (Figure 4a). In the western Weddell Sea in early summer 2004, Vihma et al. (2009) observed weak evaporation, whereas our results suggested weak condensation.

It should be noted that the observation periods have been short and sensitive to prevailing synoptic conditions, illustrated by the large synoptic-scale variability in time series of evaporation/latent heat flux (Andreas et al., 2004; Vihma et al., 2009). More observations and estimates based on different approaches are needed to establish a reliable climatology of evaporation over the Southern Ocean.

Due to the importance of water vapor in the global climate system, including its role in the Earth's surface energy budget, the water cycle, and the feedback effects related to water vapor, clouds, and radiative transfer, evaporation from the ocean surface to the atmosphere continues to be an important aspect to monitor and understand in greater detail. With the changing Antarctic sea ice extent in recent years, from increasing slightly between 1979 and 2015 to having a markedly lower maximum extents in 2016–2018, it is important to continue to monitor the changes in evaporation over the Southern Ocean and to try to understand how it will respond to the changing sea ice cover and atmospheric conditions in the future.

While these flux estimates and results are encouraging, it is essential that more in situ measurements of temperature, humidity, and winds are taken in the Southern Ocean throughout the year, and especially in those areas of the sea ice pack that are undersampled or not sampled at all because these are perhaps the areas where the largest uncertainties in AIRS and other reanalysis products occur. An improved understanding of atmospheric conditions in and around the sea ice pack of the Southern Ocean will benefit not only evaporation estimates but also our knowledge of the state and change of the climate system as a whole.

Acknowledgments

Autonomous sea ice mass balance buoy data on air temperature, humidity, and wind speed from 15 January 2016 to 1 March 2017 were obtained from http://www.meereisportal.de (grant: REKLIM-2013-04). AIRS data can be obtained at airs.jpl.nasa.gov. MERRA-2 data can be obtained from https://gmao.gsfc.nasa.gov/reanalysis/MERRA-2/data_access/. Ice concentration can be obtained from www.nsidc.org. The work of Linette Boisvert was funded by NASA GSFC Cryospheric Science Lab. The work of Timo Vihma was funded by the Academy of Finland (contract 304345). Chung-Lin Shie is a research faculty member at the Joint Center for Earth Systems Technology (JCET).

References

Andreas, E. L. (1995). Air-ice drag coefficients in the western Weddell Sea: 2. A model based on form drag and drifting snow. *Journal of Geophysical Research*, *100*, 4833–4843. https://doi.org/10.1029/94JC02016

Andreas, E. L., Claffy, K. J., & Makshtas, A. P. (2000). Low-level atmospheric jets and inversions over the western Weddell Sea. *Boundary-Layer Meteorology*, *97*(3), 459–486. https://doi.org/10.1023/A:1002793831076

Andreas, E. L., Horst, T. W., Grachev, A. A., Persson, P. O. G., Fairall, C. W., Guest, P. S., & Jordan, R. E. (2010). Parametrizing turbulent exchange over summer sea ice and the marginal ice zone. *Quarterly Journal of the Royal Meteorological Society*, *136*(649), 927–943. https://doi.org/10.1002/qj.618

Andreas, E. L., Jordan, R. E., & Makshtas, A. P. (2004). Simulations of snow, ice, and near-surface atmospheric processes on Ice Station Weddell. *Journal of Hydrometerology*, *5*(4), 611–624. https://doi.org/10.1175/1525-7541(2004)005<0611:SOSIAN>2.0.CO;2

Andreas, E. L., & Makshats, A. P. (1985). Energy exchange over Antarctic sea ice in the spring. *Journal of Geophysical Research*, *90*(C4), 7199. https://doi.org/10.1029/JC090iC04p07199

Andreas, E. L., Persson, P. O. G., Grachev, A. A., Jordan, R. E., Horst, T. W., Guest, P. S., & Fairall, C. W. (2010). Parameterizing turbulent exchange over sea ice in winter. *Journal of Hydrometeorology*, *11*(1), 87–104. https://doi.org/10.1175/2009JHM1102.1

Barber, D. G., & Massom, R. A. (2007). The role of sea ice in Arctic and Antarctic polynyas. *Elsevier Oceanography Series*, *74*, 1–54. https://doi.org/10.1016/S0422-9894(06)74001-6

Bintanja, R., & Selten, F. M. (2014). Future increases in Arctic precipitation linked to local evaporation and sea-ice retreat. *Nature*, *509*(7501), 479–482. https://doi.org/10.1038/nature13259

Boisvert, L. N., Lee, J. N., Lenaerts, J. T. M., Noel, B., van den Broeke, M. R., & Nolin, A. W. (2016). Using remotely sensed data from AIRS to estimate the vapor flux on the Greenland Ice Sheet: Comparisons with observations and a regional climate model. *Journal of Geophysical Research: Atmospheres*, *122*, 202–229. https://doi.org/10.1002/2016JD025674

Boisvert, L. N., Markus, T., Parkinson, C. L., & Vihma, T. (2012). Moisture fluxes derived from EOS Aqua satellite data for the North Water polynya over 2003-2009. *Journal of Geophysical Research*, *117*, D06119. https://doi.org/10.1029/2011JD016949

Boisvert, L. N., Markus, T., & Vihma, T. (2013). Moisture flux changes and trends for the entire Arctic in 2003-2011 derived from EOS Aqua data. *Journal of Geophysical Research: Atmospheres*, *118*, 5829–5843. https://doi.org/10.1002/jgrc.20414

Boisvert, L. N., & Stroeve, J. C. (2015). The Arctic is becoming warmer and wetter as revealed by the Atmospheric Infrared Sounder. *Geophysical Research Letters*, *42*, 4439–4446. https://doi.org/10.1002/2015GL063775

Boisvert, L. N., Wu, D. L., & Shie, C.-L. (2015). Increasing evaporation amounts seen in the Arctic between 2003-2013 from AIRS data. *Journal of Geophysical Research: Atmospheres*, *120*, 6865–6881. https://doi.org/10.1002/2015JD023258

Boisvert, L. N., Wu, D. L., Vihma, T., & Susskind, J. (2015). Verification of air/surface humidity differences from AIRS and ERA-Interim in support of turbulent flux estimation in the Arctic. *Journal of Geophysical Research: Atmospheres*, *120*, 945–963. https://doi.org/10.1002/2014JD021666

Bosilovich, M. G. and Co-Authors (2016). MERRA-2. Initial evaluation of the climate, in *Global modeling and data assimilation*, Tech. Rep. Ser., vol. 43, edited by R. D. Koster NASA/TM-2015-104606, 139 pp., Goddard Space Flight Center, Greenbelt, Md.

Bourassa, M. A., Gille, S. T., Bitz, C., Carlson, D., Cerovecki, I., Clayson, C. A., et al. (2013). High-latitude ocean and sea ice surface fluxes: Challenges for climate research. *Bulletin of the American Meteorological Society*, *94*(3), 403–423. https://doi.org/10.1175/BAMS-D-11-00244.1

Bromwich, D. H. (1989). Satellite analyses of Antarctic katabatic wind behavior. *Bulletin of the American Meteorological Society*, *70*(7), 738–749. https://doi.org/10.1175/1520-0477(1989)070<738:SAOAKW>2.0.CO%3B2

Cavalieri, D. J., Parkinson, C. L., Gloersen, P., & Zwally, H. (1996). Sea ice concentrations from Nimbus-7 SSMR and DMSP SSM/I-SSMIS passive microwave data, [2003-2016], NASA DAAC at the Natl. Snow and Ice Data Cent., Boulder, Colo. [Updated yearly].

Comiso, J. C. (2016). Global changes in the sea ice cover and associated surface temperature changes, International Archives of the Photogrammetry. *Remote Sensing & Spatial Information Sciences*, *41*.

Comiso, J. C., Parkinson, C. L., Gersten, R., & Stock, L. (2008). Accelerated decline in the Arctic sea ice cover. *Geophysical Research Letters*, *35*, L01703. https://doi.org/10.1029/2007GL031972

Cronin, M. F., Fairall, C. W., & McPhaden, M. J. (2006). An assessment of buoy derived and numerical weather prediction surface heat fluxes in the tropical Pacific. *Journal of Geophysical Research*, *111*, C06028. https://doi.org/10.1029/2005JC003324

Dong, S., Gille, S. T., Sprintall, J., & Fetzer, E. J. (2010). Assessing the potential of the Atmospheric Infrared Sounder (AIRS) surface temperature and specific humidity in turbulent heat flux estimates in the Southern Ocean. *Journal of Geophysical Research*, *115*, C05013. https://doi.org/10.1029/2009JC005542

Eastman, R., & Warren, S. G. (2010). Interannual variations of Arctic cloud types in relation to sea ice. *Journal of Climate*, *23*(15), 4216–4232 . https://doi.org/10.1175/2010JCLI3492.1

Gao, S., Chiu, L. S., & Shie, C. L. (2013). Trends and variations of ocean surface latent heat flux: Results from GSSTF2c data set. *Geophysical Research Letters*, *40*, 380–385. https://doi.org/10.1029/2012GL054620

Gelaro, R., McCarty, W., Suárez, M. J., Todling, R., Molod, A., Takacs, L., et al. (2017). The Modern-Era Retrospective Analysis for Research and Applications, version-2 (MERRA-2). *Journal of Climate*, *30*(14), 5419–5454. https://doi.org/10.1175/JCLI-D-16-0758.1

Glorsen, P., Campbell, W. J., Cavalieri, D. J., Comiso, J. C., Parkinson, C. L., & Zwally, H. J. (1992). Arctic and Antarctic sea ice, 1978–1987. Satellite Passive-Microwave Observations and Analysis, 290.

Gordon, A. (1971). Oceanography of Antarctic waters. In J. L. Reid (Ed.), *Antarctic Oceanography I*, *Antarctic Research Series* (Vol. 15, pp. 169–203). Washington, DC: American Geophysical Union.

Grachev, A. A., Andreas, E. L., Fairall, C. W., Guest, P. S., & Persson, P. O. G. (2007). SHEBA flux–profile relationships in the stable atmospheric boundary layer. *Boundary-Layer Meteorology*, *124*(3), 315–333. https://doi.org/10.1007/s10546-007-9177-6

Grosfeld, K., Treffeisen, R., Asseng, J., Bartsch, A., Bräuer, B., Fritzsch, B., et al. (2016). Online sea-ice knowledge and data platform <www.meereisportal.de>. *Polarforschung, Bremerhaven, Alfred Wegener Institute for Polar and Marine Research & German Society of Polar Research*, *85*(2), 143–155. https://doi.org/10.2312/polfor.2016.011

Hersbach, H., & Dee, D (2016). ERA5 reanalysis is in production, ECMWF Newsletter 147, ECMWF, http://www.ecmwf.inten/elibrary/16299-newsletter-nol47-spring%g-2016

Huntington, T. G. (2006). Evidence for intensification of the global water cycle: Review and synthesis. *Journal of Hydrodynamics*, *319*(1-4), 83–95. https://doi.org/10.1016/j.jhydrol.2005.07.003

Jacobs, S. S., & Comiso, J. C. (1989). Sea ice and oceanic processes on the Ross Sea continental shelf. *Journal of Geophysical Research*, *94*(C12), 18,195–18,211. https://doi.org/10.1029/JC094iC12p18195

Kay, J. E., & Gettelman, A. (2009). Cloud influence on and response to seasonal Arctic sea ice loss. *Journal of Geophysical Research*, *114*, D18204. https://doi.org/10.1029/2009JD011773

Kottmeier, C., & Engelbart, D. (1992). Generation and atmospheric heat exchange of coastal polynyas in the Weddell Sea. *Boundary-Layer Meteorology*, *60*(3), 207–234. https://doi.org/10.1007/BF00119376

Kurtz, D. D., & Bromwich, D. H. (1985). A recurring, atmospherically forced polynya in Terra Nova Bay. *Oceanology of the Antarctic Continental Shelf*, *43*, 177–201. https://doi.org/10.1029/AR043p0177

Kwok, R., & Comiso, J. C. (2002). Southern Ocean climate and sea ice anomalies associated with the Southern Oscillation. *Journal of Climate*, *15*(5), 487–501. https://doi.org/10.1175/1520-0442(2002)015<0487:SOCASI>2.0.CO;2

Kwok, R., & Rothrock, D. A. (2009). Decline in Arctic sea ice thickness from submarine and ICESat records: 1958–2008. *Geophysical Research Letters*, *36*, L15501. https://doi.org/10.1029/2009GL039035

Launiainen, J., & Vihma, T. (1990). Derivation of turbulent surface fluxes—An iterative flux-profile method allowing arbitrary observing heights. *Environmental Software*, *5*(3), 113–124. https://doi.org/10.1016/0266-9838(90)90021-W

Launiainen, J., & Vihma, T. (1994). On the surface heat fluxes in the Weddell Sea. *The Polar Oceans and Their Role in Shaping the Global Environment*, *399-419*. https://doi.org/10.1029/GM085p0399

Lindsay, R., & Schweiger, A. (2015). Arctic sea ice thickness loss determined using subsurface, aircraft, and satellite observations. *The Cryosphere*, *9*(1), 269–283. https://doi.org/10.5194/tc-9-269-2015

Liu, Y., Key, J. R., Liu, Z., Wang, X., & Vavrus, S. J. (2012). A cloudier Arctic expected with diminishing sea ice. *Geophysical Research Letters*, *39*, L05705. https://doi.org/10.1029/2012GL051251

Loaiciga, H. A., Valdes, J. B., Vogel, R., Garvey, J., & Schwarz, H. (1996). Global warming and the hydrologic cycle. *Journal of Hydrodynamics*, *174*(1-2), 83–127. https://doi.org/10.1016/0022-1694(95)02753-X

Lüpkes, C., & Gryanik, V. M. (2015). A stability-dependent parametrization of transfer coefficients for momentum and heat over polar sea ice to be used in climate models. *Journal of Geophysical Research: Atmospheres*, *120*, 1–30. https://doi.org/10.1002/2014JD022418

Maksym, T. (2019). Arctic and Antarctic Sea ice change: Contrasts, commonalities, and causes. *Annual Review of Marine Science*, *11*, 187–213. https://doi.org/10.1146/annurev-marine-010816-060610

Maslanik, J., Stroeve, J., Fowler, C., & Emery, W. (2011). Distribution and trends in Arctic sea ice age through spring 2011. *Geophysical Research Letters*, *38*, L13502. https://doi.org/10.1029/2011GL047735

Molod, A., Takacs, L., Suarez, M., & Bacmeister, J. (2015). Development of the GEOS-5 atmospheric general circulation model. Evolution from MERRA to MERRA2. *Geoscientific Model Development*, *8*(5), 1339–1356. https://doi.org/10.5194/gmd-8-1339-2015

Moore, G. W. K., Alverson, K., & Renfrew, I. A. (2002). A reconstruction of the air–sea interaction associated with the Weddell Polynya. *Journal of Physical Oceanography*, *32*(6), 1685–1698. https://doi.org/10.1175/1520-0485(2002)032<1685:AROTAS>2.0.CO;2

Morrison, A. L., Kay, J. E., Chepfer, H., Guzman, R., & Yettella, V. (2018). Isolating the liquid cloud response to recent Arctic sea ice variability using spaceborne lidar observations. *Journal of Geophysical Research: Atmospheres*, *123*, 473–490. https://doi.org/10.1002/2017JD027248

Nghiem, S. V., Rigor, I. G., Perovich, D. K., Clemente-Colón, P., Weatherly, J. W., & Neumann, G. (2007). Rapid reduction of Arctic perennial sea ice. *Geophysical Research Letters*, *34*, L19504. https://doi.org/10.1029/2007GL031138

Nicolaus, M., Hoppmann, M., Arndt, S., Hendricks, S., Katlein, C., König-Langlo, G., et al. (2017). Snow height and air temperature on sea ice from Snow Buoy measurements. *Alfred Wegener Institute, Helmholtz Center for Polar and Marine Research, Bremerhaven*. https://doi.org/10.1594/PANGAEA.875638

Ohshima, K. I., Fukamachi, Y., Williams, G. D., Nihashi, S., Roquet, F., Kitade, Y., et al. (2013). Antarctic Bottom Water production by intense sea-ice formation in the Cape Darnley polynya. *Nature Geoscience*, *6*(3), 235. https://doi.org/10.1038/ngeo1738

Palm, S. P., Strey, S. T., Spinhirne, J., & Markus, T. (2010). Influence of Arctic sea ice extent on polar cloud fraction and vertical structure and implications for regional climate. *Journal of Geophysical Research*, *115*, D21209. https://doi.org/10.1029/2010JD013900

Parkinson, C. L. (1983). On the development and cause of the Weddell Polynya in a sea ice simulation. *Journal of Physical Oceanography*, *13*(3), 501–511. https://doi.org/10.1175/1520-0485(1983)013<0501:OTDACO>2.0.CO;2

Parkinson, C. L., & Cavalieri, D. J. (2008). Arctic sea ice variability and trends, 1979–2006. *Journal of Geophysical Research*, *113*, C07003. https://doi.org/10.1029/2007JC004558

Parkinson, C. L., & Cavalieri, D. J. (2012). Antarctic sea ice variability and trends, 1979–2010. *The Cryosphere*, *6*, 871–880. https://doi.org/10.5194/tc-6-871-2012

Parkinson, C. L., & DiGirolamo, N. E. (2016). New visualizations highlight new information on the contrasting Arctic and Antarctic sea-ice trends since the late 1970s. *Remote Sensing of Environment*, *183*, 198–204. https://doi.org/10.1016/j.rse.2016.05.020

Perovich, D. K., Andreas, E. L., Curry, J. A., Eiken, H., Fairall, C. W., Grenfell, T. C., et al. (1999). SHEBA: The Surface Heat Budget of the Arctic Ocean. *Eos, Transactions of the American Geophysical Union*, *80*(41), 481–486. https://doi.org/10.1029/EO080i041p00481-01

Perovich, D. K., & Polashenski, C. (2012). Albedo evolution of seasonal Arctic sea ice. *Geophysical Research Letters*, *39*, L08501. https://doi.org/10.1029/2012gl051432

Pringle, D. J., Eicken, H., Trodahl, H. J., & Backstrom, L. G. E. (2007). Thermal conductivity of landfast Antarctic and Arctic sea ice. *Journal of Geophysical Research*, *112*, C04017. https://doi.org/10.1029/2006JC003641

Reynolds, R. W., Smith, T. M., Liu, C., Chelton, D. B., Casey, K. S., & Schlax, M. G. (2007). Daily high-resolution-blended analyses for Sea Surface Temperature. *Journal of Climate*, *20*, 5473–5496. https://doi.org/10.1175/2007JCLI1824.1

Rienecker, M. M., Suarez, M. J., Gelaro, R., Todling, R., Bacmeister, J., Liu, E., et al. (2011). MERRA. NASA's Modern-Era Retrospective Analysis for Research and Applications. *Journal of Climate*, *24*(14), 3624–3648. https://doi.org/10.1175/JCLI-D-11-00015.1

Rinke, A., Melsheimer, C., Dethloff, K., & Heygster, G. (2009). Arctic total water vapor: Comparison of regional climate simulations with observations, and simulated decadal trends. *Journal of Hydrometeorology*, *10*(1), 113–129. https://doi.org/10.1175/2008JHM970.1

Serreze, M. C., Barrett, A. P., Kindig, D. N., & Holland, M. M. (2009). The emergence of the surface-based Arctic amplification. *The Cryosphere*, *3*, 11–19. https://doi.org/10.5194/tc-3-11-2009

Serreze, M. C., & Meier, W. N. (2018). The Arctic's sea ice cover: Trends, variability, predictability, and comparisons to the Antarctic. *Annals of the New York Academy of Sciences*, *1436*(1), 36–53. https://doi.org/10.1111/nyas.13856

Smith, S. D., Muench, R. D., & Pease, C. H. (1990). Polynyas and leads: An overview of physical processes and environment. *Journal of Geophysical Research*, *95*(C6), 9461–9479. https://doi.org/10.1029/JC095iC06p09461

Susskind, J., Blaisdell, J. M., & Iredell, L. (2014). Improved methodology for surface and atmospheric soundings, error estimates, and quality control procedures: The atmospheric infrared sounder science team version-6 retrieval algorithm. *Journal of Applied Remote Sensing*, *8*(1), 084994. https://doi.org/10.1117/1.JRS.8.084994

Tastula, E.-M., Vihma, T., Andreas, E. L., & Galperin, B. (2013). Validation of the diurnal cycles in atmospheric reanalyses over Antarctic sea ice. *Journal of Geophysical Research: Oceans*, *118*, 4194–4204. https://doi.org/10.1002/jgrd.50336

Taylor, P., Hegyi, B., Boeke, R., & Boisvert, L. (2018). On the increasing importance of air-sea exchanges in a thawing Arctic: A review. *Atmosphere*, *9*(2), 41. https://doi.org/10.3390/atmos9020041

Taylor, P. C., Kato, S., Xu, K. M., & Cai, M. (2015). Covariance between Arctic sea ice and clouds within atmospheric state regimes at the satellite footprint level. *Journal of Geophysical Research: Atmospheres*, *120*, 12,656–12,678. https://doi.org/10.1002/2015JD023520

Tietäväinen, H., & Vihma, T. (2008). Atmospheric moisture budget over Antarctica and Southern Ocean on the basis of ERA-40 reanalysis. *International Journal of Climatology*, *28*, 1977–1995. https://doi.org/10.1002/joc.1684

Trenberth, K. E. (1999). *Conceptual framework for changes of extremes of the hydrological cycle with climate change, In Weather and Climate Extremes* (pp. 327–339). Dordrecht: Springer. https://doi.org/10.1007/978-94-015-9265-9_18

Turner, J., Hosking, J. S., Bracegirdle, T. J., Marshall, G. J., & Phillips, T. (2015). Recent changes in Antarctic sea ice. *Philosophical Transactions of the Royal Society A: Mathematical, Physical and Engineering Sciences*, *373*(2045). https://doi.org/10.1098/rsta.2014.0163

Vihma, T., Johansson, M. M., & Launiainen, J. (2009). Radiative and turbulent surface heat fluxes over sea ice in the western Weddell Sea in early summer. *Journal of Geophysical Research*, *114*, C04019. https://doi.org/10.1029/2008JC004995

Vihma, T., Screen, J., Tjernström, M., Newton, B., Zhang, X., Popova, V., et al. (2016). The atmospheric role in the Arctic water cycle: A review on processes, past and future changes, and their impacts. *Journal of Geophysical Research: Biogeosciences*, *121*, 586–620. https://doi.org/10.1002/2015JG003132

Vihma, T., Uotila, J., Cheng, B., & Launiainen, J. (2002). Surface heat budget over the Weddell Sea: Buoy results and model comparisons. *Journal of Geophysical Research*, *107*(C2), 3013. https://doi.org/10.1029/2000JC000372

Wendler, G., Hartmann, B., Wyatt, C., Shulski, M., & Stone, H. (2005). Midsummer energy balance for the southern seas. *Boundary-Layer Meteorology*, *117*(1), 131–148. https://doi.org/10.1007/s10546-004-7090-9

Wyser, K., Jones, C. G., Du, P., Girard, E., Willén, U., Cassano, J., et al. (2008). An evaluation of Arctic cloud and radiation processes during the SHEBA year: Simulation results from eight Arctic regional climate models. *Climate Dynamics*, *30*, 203–223. https://doi.org/10.1007/s00382-007-0286-1

Zhang, J. (2007). Increasing Antarctic sea ice under warming atmospheric and oceanic conditions. *Journal of Climate*, *20*(11), 2515–2529. https://doi.org/10.1175/JCLI4136.1

Zwally, H. J., Comiso, J. C., & Gordon, A. L. (1985). Antarctic offshore leads and polynyas and oceanographic effects. *Oceanology of the Antarctic Continental Shelf*, *43*, 203–226. https://doi.org/10.1029/AR043p0203